FERMI-LAT AND CHANDRA STUDIES OF SHELL LIKE SUPERNOVA REMNANTS

by

Mustafa Bozkurt

B.S., Integrated B.S and M.S Program in Teaching Physics, Boğaziçi University, 2009

Submitted to the Institute for Graduate Studies in
Science and Engineering in partial fulfillment of
the requirements for the degree of
Master of Science

Graduate Program in Physics
Boğaziçi University

2012

ACKNOWLEDGEMENTS

I would like to express my sincere appreciation to my thesis advisor Prof. Enise Nihal Ercan for her support, encouragement, and guidance throughout this study. I am in debt for her generous sharing of knowledge and expertise. One simply could not wish for a friendlier supervisor. I will always remember her warm personality and enthusiasm.

I also owe thanks to the mentor of this thesis Tülün Ergin for her valuable guidance for every step of this study. Without her trust in me, this thesis count not have been accomplished. She offered invaluable assistance and support for this study. I will always appreciate her effort for this thesis.

I would like to thank my friend Esra for her support and patience for all my graduate education.

Being a research assistant in Department of Secondary School Science and Mathematics Education brought enthusiasm and happiness to me. I feel lucky to have worked here. I want to thank all SCED department for their understanding and contributions to improve my academic career.

I wish to express my gratitude to Murat Hüdaverdi for his precious guidance and constructive feedbacks greatly contributing to this study. I would like to thank for his endless support to every aspects of my life. I have learned a lot from him.

I also wish to express my deepest thanks to my sister and my mother for their endless love, support, understanding and trust throughout my life. They taught me to trust in myself and to stand strongly wherever I am. Thank you for always being in my life.

to my father

ABSTRACT

FERMI-LAT AND CHANDRA STUDIES OF SHELL LIKE SUPERNOVA REMNANTS

Supernova Remnants (SNRs) have long been considered to be the primary source of galactic cosmic rays (CRs) having energies below the so called "knee", $\sim 10^{15}$ eV. CRs are accelerated by SNRs which transfer some of their internal energies into charged particles. Those charged particles in SNRs produce high energy photons up to TeV energies. Main motivation of this study is to investigate young, shell-like SNRs as high energy (HE) sources and to better understand the origins of main HE emissions. SNRs are observable in GeV energies by means of Fermi Gamma Ray Space Telescope (Fermi). Generally, there are two accepted models for the gamma-ray production in SNRs: (i) The leptonic model, where emission arises from inverse Compton and relativistic bremsstrahlung, (ii) the hadronic model, where gamma rays are produced from decay of neutral pions originating from proton-proton interactions. Fermi analysis of SNRs, Cassiopeia A (Cas A) and Tycho as point-like sources in gamma-ray, has shown that these young SNRs are GeV sources in the Milky Way. Also, about half of the SNRs in the galaxy are observed in the X-ray band [16]. The X-ray emission of SNRs results from the interactions of ejecta of the SNR and swept-up interstellar medium (ISM). Bremsstrahlung and line emissions are the thermal and main X-ray emission mechanisms in SNRs. Synchrotron emission is the non-thermal contribution of X-ray emission and it is produced by charged particles in strong magnetic field. Chandra-ACIS image and spectral analysis of Cas A and Tycho was performed both to understand shell-like structures of SNRs and, to examine which part of SNRs are responsible for main non-thermal emission. Also Chandra analysis showed that thin filaments at the shell of the remnants associated with reverse shocks are the most important candidate regions, where non-thermal emission is dominant.

ÖZET

KABUKSU YAPILI SÜPERNOVA KALINTILARININ FERMI-LAT VE CHANDRA ÇALIŞMALARI

Süpernova kalıntıları (SNK'lar), enerjileri $\sim 10^{15}$ eV seviyesi ve altındaki galaktik kozmik ışınların (KI) öncelikli kaynağı olarak düşünülmektedir. Kozmik ışınlar, SNK'ların iç enejilerinin bir bölümünü bu yüklü parçacıklara aktarması ile ivme kazanırlar. Süpernova kalıntılarında ki bu yüklü parçacıklar TeV mertebesinde yüksek enerjili fotonları üretirler. Bu çalışmadaki esas amaç genç, kabuksu SNK'ları, yüksek enerji kaynakları (YE) olarak incelemek ve X ve gama ışımalarının SNK'nın hango bölgelerinden geldiğini anlamaktır. SNK'lar Fermi Gama Ray Space Teleskopu (Fermi) ile GeV enerjilerinde gözlemlenebilmektedir. SNK'larda gama ışını üretimi için genel olarak kabul edilmiş iki model bulunmaktadır: (i) Ters Compton ve relativistik bremsstrahlung süreçleri ile gama ışımasının meydana geldiği Leptonik Model, ve (ii) Proton-proton etkileşimi ile oluşan nötr pionların bozulması ile gama ışını üretiminin yapıldığı Hadronik Model. Gama ışın dalga boylarında noktasal kaynaklar olan Cassiopeia A (Cas A) ve Tycho'nun galaktik gama ışın kaynakları olduklarını gözlemsel olarak göstermek için Fermi analizleri gerçekleştirildi. Ayrıca, galaksimizdeki SNK'ların yaklaşık yarısı X-ışın bandında da gözlemlenmiştir [16]. SNK'larda X-ışın üretiminin temel süreci, süpernova patlamasıyla dışarı atılan madde ile dışarda süpürülen yıldızlar arası ortamın etkileşimidir. Bu süreçte Bremsstrahlung ve çizgi ışımaları SNK'larda ki temel termal X-ışın üretim mekanizmalarıdır. Yüklü parçacıkların güçlü manyetik alan içerisindeki hareketi ile oluşan synchrotron ışıması ise SNK'larda ki X-ışının üretiminde termal olmayan ışımadan sorumludur. Bu tezde, Fermi analizlerinin yanı sıra, SNK'ların kabuksu yapılarını anlamak ve SNK'ların hangi bölümlerinin termal olmayan ışımanın temel kaynağı olduğunu araştırmak için Chandra-ACIS ile Cas A ve Tycho'nun görüntü ve tayf analizleri yapılmıştır.

TABLE OF CONTENTS

ACKNOWLEDGEMENTS iii
ABSTRACT v
ÖZET vi
LIST OF FIGURES x
LIST OF TABLES xiv
LIST OF SYMBOLS xvi
LIST OF ACRONYMS/ABBREVIATIONS xviii
1. INTRODUCTION 1
2. SUPERNOVA REMNANTS 3
2.1. Evolution of SNRs 3
2.1.1. Free Expansion Phase 3
2.1.2. Transition Phase 3
2.1.3. Adiabatic (Sedov) Phase 4
2.1.4. Radiative Cooling Phase 4
2.2. Types of SNRs 4
2.2.1. Shell-like SNRs 5
2.2.2. Plerion Type of SNRs 5
2.2.3. Composite SNRs 6
2.2.4. Mixed-Morphology SNRs 6
3. COSMIC RAY ACCELERATION & HIGH ENERGY EMISSION FROM SNRs 9
3.1. Cosmic Ray Acceleration from Supernova Remnants 9
3.1.1. Diffuse Shock Acceleration - Fermi Mechanism 10
3.2. Gamma Ray Emission Mechanism from SNRs 13
3.2.1. Leptonic Origin of Gamma Rays 13
3.2.1.1. Relativistic Bremsstrahlung 13
3.2.1.2. Inverse Compton Process 14
3.2.2. Hadronic Origin of Gamma Rays 14
3.2.2.1. Production and Decay of Neutral Pions 14
3.3. X-ray Emission Mechanism from SNRs 15

3.3.1. Thermal Bremsstrahlung Emission 16
3.3.2. Radiative Recombination 16
3.3.3. Line Emissions 16
3.3.4. Synchrotron Radiation 18
3.3.5. Thin Thermal Plasma in SNRs 20
3.3.5.1. Ionizing Plasma ($kTe > kTz$) 20
3.3.5.2. Equilibrium Plasma (kTe = kTz) 20
3.3.5.3. Recombining Plasma ($kTe < kTz$) 21
4. INSTRUMENTS 22
4.1. Fermi Gamma Ray Space Telescope 22
4.1.1. Overview and Mission 22
4.1.2. Large Area Telescope - LAT 23
4.1.2.1. The Anti-Coincidence Detector - ACD 23
4.1.2.2. The Tracker 26
4.1.2.3. The Calorimeter 26
4.1.2.4. Data Acquisition System 27
4.1.3. Gamma-ray Burst Monitor - GBM 27
4.1.3.1. Low Energy Detectors 27
4.1.3.2. High Energy Detectors 27
4.1.3.3. Data Processing Unit 27
4.2. Chandra X-ray Observatory 28
4.2.1. X-ray Telescope 28
4.2.2. The Science Instruments 28
4.2.2.1. Advanced CCD Imaging Spectrometer - ACIS 29
4.2.2.2. High Resolution Camera -HRC 30
4.2.2.3. HETG and LETG Spectrometers 30
4.2.3. Spacecraft 31
5. ANALYSIS & RESULTS 32
5.1. CASSIOPEIA A 32
5.1.1. Overview of the Previous Results of Cas A 32
5.1.2. Fermi-LAT Analysis of Cas A 33

5.1.2.1. Data Preparation 33
5.1.2.2. Creating Count Cube and Map 33
5.1.2.3. Building Background Model 34
5.1.2.4. Computing Exposures and Source Map 34
5.1.2.5. Binned Likelihood Analysis of Cas A 35
5.1.2.6. Fermi Analysis Results of Cas A 36
5.1.3. Chandra X-ray Analysis of Cas A 36
5.1.3.1. Data Reduction 36
5.1.3.2. Image Analysis of Cas A 39
5.1.3.3. Spectral Analysis of Cas A 40
5.2. TYCHO 53
5.2.1. Overview of the Previous Results of Tycho 53
5.2.2. Fermi-LAT Analysis of Tycho 53
5.2.2.1. Data Preparation 54
5.2.2.2. Creating Count Cube and Map 54
5.2.2.3. Building Background Model 55
5.2.2.4. Computing Maps and Binned Likelihood Analysis . . . 55
5.2.2.5. Fermi Analysis Results of Tycho 56
5.2.3. Chandra Analysis of Tycho 57
5.2.3.1. Data Reduction 57
5.2.3.2. Image Analysis of Tycho 57
5.2.3.3. Spectral Analysis of Tycho 57
6. SUMMARY AND DISCUSSION 71
REFERENCES 73

LIST OF FIGURES

Figure 2.1. Chandra true color image of the shell-like SNR Kepler. 5

Figure 2.2. Chandra true color image of a plerion type SNR, the Crab Nebula. 6

Figure 2.3. Chandra true color image of composite SNR Kes 75. 7

Figure 2.4. Chandra true color image of composite SNR 3C 391. 8

Figure 3.1. Cosmic ray spectrum. Y-axis shows flux of cosmic rays coming from a variety of sources hitting on the surface of the Earth, and x-axis shows energies of cosmic rays. 9

Figure 3.2. Shock Front. 11

Figure 3.3. Helical motion of an electron in uniform magnetic field. 19

Figure 4.1. GeV gamma-ray sky. Color scale shows number of photons with energy greater than 1 GeV detected per pixel in the first 2 years of LAT operation. 23

Figure 4.2. Fermi LAT design. Figure is taken from Atwood *et al.* [21]. 24

Figure 4.3. LAT schematic view. Yellow layers show ACD. The figure is taken from Atwood *et al.* [21]. 26

Figure 4.4. Gamma-ray Bburst sky. 264 GRBs (in red) in the field of view of LAT out of total 514. GRB2010 conference results Annapolis, 2010. 28

Figure 4.5. Chandra X-ray Observatory view. 29

Figure 4.6. ACIS CCD design. 30

Figure 4.7. Schematic view of grating spectrometers. 31

Figure 5.1. Cas A counts map smoothed with 3σ and in the energy range of 0.2-300 GeV. 34

Figure 5.2. Fermi gamma-ray energy spectrum of Cas A. 36

Figure 5.3. Fermi gamma-ray Flux vs Energy spectrum of Cas A. 37

Figure 5.4. Fermi gamma-ray Count Spectrum of Cas A. 37

Figure 5.5. Cas A Chandra soft energy X-ray image in the range of 0.3 - 1.5 keV. 40

Figure 5.6. Cas A Chandra medium energy X-ray image in the range of 1.5 - 2.5 keV. 41

Figure 5.7. Cas A Chandra hard energy X-ray image in the range of 2.5 - 8.0 keV. 41

Figure 5.8. Cas A Chandra image in the range of 0.3 - 8 keV. 42

Figure 5.9. Cas A Chandra combined image of soft, medium and hard energies. 42

Figure 5.10. Cas A combined image with selected regions. Elliptical areas show the regions that spectral analysis were performed on. 43

Figure 5.11. X-ray spectrum of the northwest region of Cas A. 45

Figure 5.12. X-ray spectrum of the northeast region of Cas A. 46

Figure 5.13. X-ray spectrum of the southeast region of Cas A. 47

Figure 5.14. X-ray spectrum of the south region of Cas A. 48

Figure 5.15. X-ray spectrum of the southwest region of Cas A. 49

Figure 5.16. X-ray image of Cas A with regions selected inside. 50

Figure 5.17. Chandra X-ray spectrum of inside region 1 and 2 of Cas A, top and bottom panels, respectively. 51

Figure 5.18. Chandra X-ray spectrum of inside region 3 and 4 of Cas A, top and bottom panels, respectively. 52

Figure 5.19. Fermi $8^o \times 8^o$ counts map of Tycho smoothed with 3σ in the energy range of 0.2 - 200 GeV. 54

Figure 5.20. Residual map of Tycho smoothed with 3σ. The left map was built with background XML model file including Tycho. The right map was built with background XML file not including Tycho. The difference shows the detection of Tycho. The residuals are ranging between -6.5 and +6.5 counts and Tycho is visible in the range of +0.9 - +5.8 counts. 56

Figure 5.21. Tycho Chandra soft energy image in the range of 0.3 - 1.5 keV. . . 58

Figure 5.22. Tycho Chandra medium energy image in the range of 1.5 - 2.5 keV. 58

Figure 5.23. Cas A Chandra hard energy image in the range of 2.5 - 8 keV. . . 59

Figure 5.24. Tycho Chandra image in the range of 0.3 - 8 keV. 59

Figure 5.25. Tycho Chandra combined image of soft, medium, and hard energies with selected regions. 60

Figure 5.26. X-ray spectrum of the east region of Tycho. 61

Figure 5.27. X-ray spectrum of the north region of Tycho. 62

Figure 5.28. X-ray spectrum of the northeast region of Tycho. 63

Figure 5.29. X-ray spectrum of the south region of Tycho. 64

Figure 5.30. X-ray spectrum of the southeast region of Tycho. 65

Figure 5.31. X-ray spectrum of the southwest region of Tycho. 66

Figure 5.32. X-ray spectrum of the west region of Tycho. 67

Figure 5.33. The Chandra combined image of soft, medium, and hard energies with selected regions from Tycho. 68

Figure 5.34. Chandra X-ray spectrum of inside regions 1 and 2 of Tycho, top and bottom panels, respectively. 69

Figure 5.35. Chandra X-ray spectrum of inside regions 3 and 4 of Tycho, top and bottom panels, respectively. 70

LIST OF TABLES

Table 3.1. H-like emission lines energies of some elements mostly observed in SNRs in eV [44]. 17

Table 3.2. He-like emission lines energies for Heα transitions of some elements mostly observed in SNRs in eV [44]. 18

Table 3.3. He-like emission lines energies for Heβ and Heγ transitions of some elements mostly observed in SNRsin eV [44]. 18

Table 4.1. LAT comparison with previous experiments. 24

Table 4.2. Sources of Fermi 2nd year catalog results [22]. 25

Table 5.1. Background point sources located within the radius of 10^o around the location of Cas A. 35

Table 5.2. Best fit spectral values of the northwest region of Cas A. 46

Table 5.3. Best fit spectral values of the northeast region of Cas A. 47

Table 5.4. Best fit spectral values of the southeast region of Cas A. 48

Table 5.5. Best fit spectral values of the south region of Cas A. 49

Table 5.6. Best fit spectral values of the southwest region of Cas A. 50

Table 5.7. Background point sources located within the radius of 6^o around the location of Tycho. 55

Table 5.8. Best fit spectral values of the east region of Tycho. 61

Table 5.9. Best fit spectral values of the north region of Tycho. 62

Table 5.10. Best fit spectral values of the northeast region of Tycho. 63

Table 5.11. Best fit spectral values of the south region of Tycho. 64

Table 5.12. Best fit spectral values of the southeast region of Tycho. 65

Table 5.13. Best fit spectral values of the southwest region of Tycho. 66

Table 5.14. Best fit spectral values of the west region of Tycho. 67

LIST OF SYMBOLS

A(E)	Energy Distribution in Power Law
Ar	Argon
c	Speed of Light
Ca	Calcium
e	Charge Unit
E	Energy
E_l	Line energy
eV	Electron Volt
Fe	Iron
GeV	Giga Electron Volt
g_{ff}	Gaunt Factor
K	Norm
kT_e	Temperature of Electron
kT_z	Ionization Temperature
K_T	Total Photon Counts
Lyα	H-like Kα
Lyβ	H-like Kβ
Lyγ	H-like Kγ
m_e	Mass of Electron
M(E)	Energy Distribution in Wabs Model
M_{Ej}	Mass of Ejecta
M_{ISM}	Mass of ISM
m_p	Mass of Proton
m_{π^0}	Mass of Neutral Pion
Mg	Magnesium
n	Electron Density
n_i	Ion Density
n_H	Hydrogen Column Density

p	Momentum
P	Pressure
P_{shock}	Probability of remaining in shock region
P_{syn}	Power
r_0	Radius of helical path
S	Sulfur
Si	Silicon
t	Time
TeV	Tera Electron Volt
U_B	Magnetic Energy Density
U_{rad}	Energy Density of Radiation
v	velocity
v_e	Velocity of Electron
V	Volume
w	Frequency
W	Power per unit time
W'	Power per unit time (relativistic)
Z	Atomic Number
α	Photon Index
γ	Lorentz Factor
σ	Significance
σ_T	Cross Section
σ_w	Line Width
σ_E(E)	Photo-electric Cross Section
χ^2/dof	Chi Squared per Degree of Freedom
π^0	Neutral Pion

LIST OF ACRONYMS/ABBREVIATIONS

ACD	The Anti-Coincidence Detector
ACIS	Advanced CCD Imaging Spectrometer
ASCA	Advanced Satellite for Cosmology and Astrophysics
BI	Back illuminated
Cas A	Cassiaopeia A
CCD	Charge Coupled Device
CIE	Collisional Ionization Equilibrium
CNRS	Centre National de la Recherche Scientifique
CR	Cosmic Rays
CXO	The Chandra X-ray Observatory
DSA	Diffuse Shock Acceleration
FI	Front Illuminated
EGRET	Energetic Gamma Ray Experiment Telescope
GRB	Gamma-ray Burst Monitor
GTI	Good Time Interval
ISM	Interstellar Medium
HE	High Energy
HEASOFT	High Energy Astrophysics Software
H.E.S.S.	High Energy Stereoscopic System
HETG	The High Energy Transmission Grating
HRC	High Resolution Camera
HRMA	High Resolution Mirror Assembly
KI	Kozmik Işın
LAT	Large Area Telescope
LETG	The Low Energy Transmission Grating
NASA	National Aeronautics and Space Administration
PH	Photon Database
PSF	point spread function

ROI	Region of Interest
SC	Specraft Pointing Including Livetime and History Database
SN	Supernova
SNR	Supernova Remnant
SNK	Süpernova Kalıntısı
TS	Test Statistics
VERITAS	The Very Energetic Radiation Imaging Telescope Array System
YE	Yüksek Enerji

1. INTRODUCTION

A supernova (SN) explosion, as one of the most energetic events in the universe, results in structures, called a supernova remnant (SNR), while releasing tremendous amount of energy ($\sim$1-2$\times10^{44}$ J) into the space. SNRs are objects, which are so energetic that they can be accepted as the main HE sources to accelerate particles up to TeV energies. The origin and acceleration mechanism of cosmic rays at these energies have been a long-standing mystery since the discovery of cosmic rays [61]. Observations of X-ray synchrotron emission from shock front of SNR Tycho [2] has brought the idea that shocks of SNRs would be cosmic ray accelerators. X-ray synchrotron radiation is an evidence for relativistic cosmic ray electrons. After Tycho, G347.3-0.5 [3], RCW 86 [4], G266.6-1.2 [3] have been categorized into synchrotron X-rays emitting SNRs [5]. ASCA Galactic plane survey has made contributions to studies of SNRs with synchrotron X-rays [5]. Recently a significant number of SNRs having dominant non-thermal emissions especially from their shells have been revealed by Chandra X-ray Observatory. Additionally, Fermi Gamma-ray Space Telescope [46], [57] and ground-based Cherenkov telescopes, such as VERITAS [58] and H.E.S.S. [61] also observed TeV gamma rays from the shell of SNRs.These findings have provided reasonable evidences for the cosmic ray acceleration at the shocked shell of SNRs. The most conceivable model to explain cosmic ray acceleration is the diffuse shock acceleration (DSA) theory of Bell [7]. According to this process, particles can be accelerated by the shock into a power-law distribution. However, there are still many significant problems about cosmic ray acceleration, because dynamical evolution of an SNR affects cosmic ray acceleration process (e.g., explosion energy, mass of ejecta, ambient density) [42]. We still lack the information about the maximum energy of particles, the configuration of magnetic fields, the injection efficiency from thermal plasma, and the acceleration history of particles around the shock fronts.

In this thesis, the young SNRs Cas A (SN explosion observed in 1680) and Tycho (SN explosion observed in 1572) were selected to understand the nature of the HE emission from SNRs. These two SNRs have been preferred in the thesis, since the

charged particles responsible for HE emission are still energetic in such young, shell-like SNRs. We concentrated on X-ray and gamma ray analysis of the remnants to determine the origins of the high energy emissions of Cas A and Tycho. Fermi analysis of such shell-like SNRs reveals significant emissions at GeV energies. The strong detection of SNRs at such GeV energies shows that SNRs are important candidates of galactic cosmic ray accelerations in the Milky Way. Besides, in order to determine which regions of the SNRs have dominant non-thermal emissions, SNRs having extended emissions (shell-like structures) in the X-ray were selected. Cas A and Tycho are suitable candidates for this criteria. In SNRs, synchrotron emissions are the non-thermal X-ray emission mechanisms responsible for the higher energy slice in X-ray spectrum (2.5 - 8 keV). Emitting regions related to these energies (called hard X-ray) of synchrotron emission are found in thin areas, called filaments, about 0.01-0.4 pc [5] at the shell of the remnants. This non-thermal emission can be best fitted with power-law model. For both SNRs, we first worked on Chandra X-ray spectral analysis of 12 thin filaments (5 for Cas A and 7 for Tycho) associated with forward shock regions at the shells. We generated a spectrum for each region fitted with power-law model and added some gaussian components for line emissions. However, as expected, the spectrums of 8 regions selected inside the SNRs could not be fitted by the non-thermal power-law model. So, the Chandra study of young SNRs clearly support the mechanism of DSA responsible for particles being accelerated up to high energies.

2. SUPERNOVA REMNANTS

Supernova remnants (SNRs) are the resulting structures of the supernova (SN) explosions. 274 SNRs are identified in the Galaxy according to the Green's Catalog 2009, and about a half of them are observed in X-rays. Evolution of SNRs is mainly determined by the ratio between the mass of material ejected by the SN explosion and the mass of swept-up interstellar matter (ISM). There are 4 phases describing different stages of SNRs. The density of the ambient medium is assumed to be uniform. In this chapter, the evolutionary processes and types of SNRs are summarized.

2.1. Evolution of SNRs

2.1.1. Free Expansion Phase

This is the earliest stage of a SNR. At the beginning of this stage, the mass of swept-up ISM (M_{ISM}) is not comparable with the mass of ejecta (M_{Ej}), in other words M_{ISM} is negligible to M_{Ej}. The majority of the energy (97 - 98%) coming from the SN explosion is released kinetically, the rest is converted to thermal energy. The free expansion phase typically takes a few hundred years. The lower the ambient density gets the longer the timescale becomes. At the end of this stage, M_{ISM} is considered to be close to M_{Ej}.

2.1.2. Transition Phase

This is the transition phase between the free expansion and the adiabatic stages. Most of the SNRs, such as Cas A and Tycho, are considered to be in this phase. M_{ISM} is comparable to M_{Ej}. SN explosion creates blast shock propagating outward, called forward shock. Ejected material arising from SN is decelerated by swept-up interstellar matter. It produces another shock wave propagating inward, called reverse shock. Between these two shock waves, interaction of swept-up ISM and ejected materials produces non-thermal dominated X ray emission and forms a bright shell-like structure.

However, the central region is still not hot enough to strongly emit X-ray [15].

2.1.3. Adiabatic (Sedov) Phase

This stage describes the condition that M_{Ej} is much smaller than M_{ISM}. The loss of energy with radiation is negligible to initial energy, so it is called adiabatic phase. The density of ejecta is much smaller than that of the swept-up ISM, therefore, main X-ray emission is produced from M_{ISM}. Adiabatic phase typically takes a few ten thousands years. About 70% of the initial explosion energy is converted into thermal energy of swept-up ISM at the end of this phase.

2.1.4. Radiative Cooling Phase

In this stage evolution of SNR is no longer adiabatic, because of increasing cooling rate. As temperature decreases, the pressure in the shell becomes lower. Then materials in the shell are compressed more, so it creates a dense shell. But the interior region still expands adiabatically. Thus, the shell is driven by the pressure of the internal gas according to $PV^{\varphi} = \text{const.}$, where P and V are the mean pressure and the volume of the internal gas respectively, and φ is the specific heat ratio. As the velocity of blast shock becomes close to speed of ISM, SNR loses its boundary. This is the end of the SNR evolution, called Disappearance Phase.

2.2. Types of SNRs

SNRs are classified by their radio and X-ray structures. There are 4 main types of SNRs in terms of their structures, which are shell-like, plerion, composite, and mixed morphology. In this chapter, SNRs are categorized with respect to their X-ray and radio emission forms [16].

2.2.1. Shell-like SNRs

These type of SNRs have bright X-ray and radio images, but there is no bright emission associated with central region. Generally SNRs in this category are considered to be in the transition phase between free expansion and adiabatic phases. Electrons accelerated to the GeV energies are the main sources of non-thermal radio emission. Therefore, it is expected to observe such SNRs in gamma rays. Nearly 65% of galactic SNRs are considered to be in this type. Most typical shell-like SNRs are Cassiopeia A, Tycho, RX J1713.7-3946, and Kepler. Figure 2.1 shows the shell-like SNR Kepler [52].

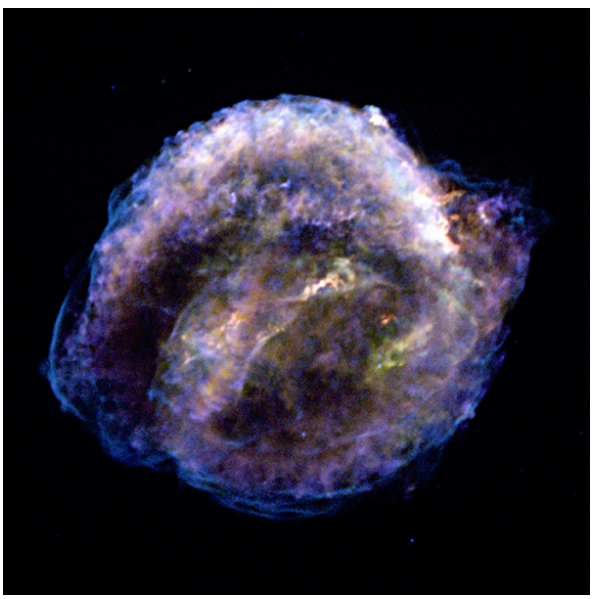

Figure 2.1. Chandra true color image of the shell-like SNR Kepler.

2.2.2. Plerion Type of SNRs

Plerion type SNRs, also called Crab-like SNRs, have non-thermal central emission in radio and X-ray. Synchrotron emission is the origin of X-ray emission observed in the central region. Almost 4% of galactic SNRs have Crab-like structures. The Crab Nebula (Figure 2.2) [52] and 3C 58 are typical examples of these of SNRs where relativistic electrons are produced by compact object.

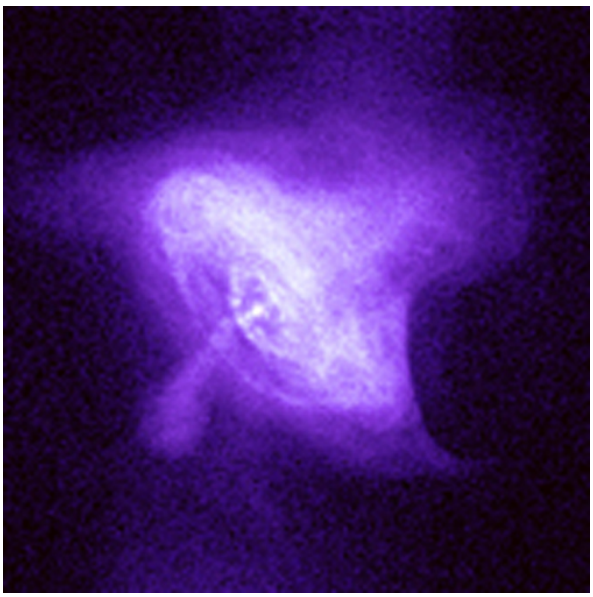

Figure 2.2. Chandra true color image of a plerion type SNR, the Crab Nebula.

2.2.3. Composite SNRs

Those are the mixture of the shell type and plerion type remnants. They have both bright central and shell emissions in radio and X-ray. Central and shell emissions are generally associated with pulsar and blast wave, respectively. Composite SNRs constitute about 10% of galactic SNRs. CTB 109 and Kes 75 (Figure 2.3) [52] are the best known examples.

2.2.4. Mixed-Morphology SNRs

Mixed-morphology type was first suggested by Rho & Petre in 1998 [13]. This type of remnants have shell-like morphology in radio band and center-filled structure in X-ray. Cloud evaporation and fossil conduction [13] models were to explain this type. Cloud evaporation model shortly claims that interior clouds evaporate and emit X rays. On the other hand, fossil conduction model assumes that such mixed morphology SNRs have hot interior plasma gradually becoming uniform by thermal conduction and produces centrally bright X-ray structure. Also X-ray produced in the shell is absorbed by ISM, because of low temperature. Nearly 10% of galactic SNRs and almost 25% of

Figure 2.3. Chandra true color image of composite SNR Kes 75.

galactic SNRs observed in X-ray are of this type. 3C 391 (Figure 2.4) [52], IC 443, and W 44 are in this group.

Figure 2.4. Chandra true color image of composite SNR 3C 391.

3. COSMIC RAY ACCELERATION & HIGH ENERGY EMISSION FROM SNRs

3.1. Cosmic Ray Acceleration from Supernova Remnants

Cosmic rays consist of protons, electrons, helium ions, and heavy nuclei and reach energies up to 10^{21} eV. Cosmic rays having energies below 10^{15} eV are considered to be of galactic origin. The higher energy cosmic rays ($> 10^{18}$ eV) are thought to be of extragalactic origin. There are also several ideas that cosmic rays having 10^{20} eV may be triggered by shocks in gamma bursts [9]. Figure 3.1 shows the spectrum of cosmic rays hitting the surface of the Earth [51].

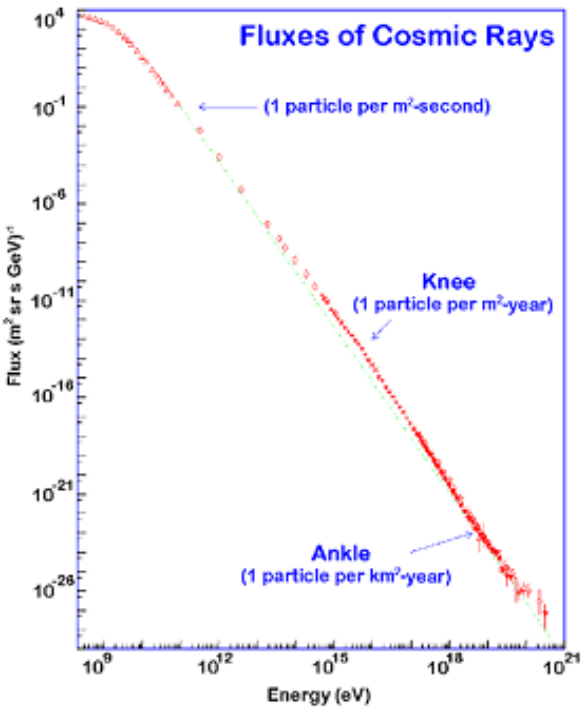

Figure 3.1. Cosmic ray spectrum. Y-axis shows flux of cosmic rays coming from a variety of sources hitting on the surface of the Earth, and x-axis shows energies of cosmic rays.

The question of how these energetic particles are produced is still being debated. Most promising candidates of galactic sources are supernova remnants, because they are energetically favorable and they can also provide mechanisms to accelerate particles to high energies through the diffuse shock acceleration. The theory of diffusive shock acceleration of cosmic rays claims that shock energy from supernova explosion increases the magnetic field around it and this amplified magnetic field accelerates the particles [7]. Tycho and Cas A are core collapse supernova types and their corresponding effective downstream magnetic field values are between 240 μG and 360 μG, [59]. Such amplification process naturally produces power-law cosmic ray distributions. Firstly radio observations support the relation between SNRs and high energy electrons by synchrotron emission [12]. Radio emission from SNRs exhibits that cosmic-rays, at least electrons, are being accelerated in those turbulent objects [11]. X-ray observations by Chandra X-ray Observatory clearly reveal the existence of such high energy electrons within SNRs. These energetic electrons produce thin X-ray filaments on the shell of the remnant associated with the front shocks. X-ray spectrum of the filaments shows power-law distribution of particles as they move in amplified magnetic field.

In spite of the findings about the relation between high energy electrons and SNRs, there is still no direct evidence of acceleration of the particles from SNRs. In order to comprehend how these particles gain such energies via cosmic ray acceleration from SNRs, we should examine gamma ray production mechanisms from SNRs, which are called the hadronic and the leptonic emission mechanism. Since GeV emission is produced either by neutral pions, created in proton-proton interactions, or relativitstic electrons, it is necessary to understand the relation between gamma ray emission and accelerated high energy electrons and protons.

3.1.1. Diffuse Shock Acceleration - Fermi Mechanism

Fermi (1949) postulated that energetic cosmic rays could be created with the diffusion between collisions and interstellar clouds colliding in space. Diffuse shock acceleration is also called the First Order Fermi Mechanism. In the Milky Way, there are several sources for shock acceleration: stellar winds, supernova remnants, or accreting

X-ray binaries, etc. The Fermi mechanism is applied to collisionless shock where the mean free path of particles is much larger than length scale of shock transition. In SNRs, charged particles can gain energy by crossing the shock repeatedly. Consider the case that a charged particle moving velocity of v_0 through a shock wave, and the direction of particle is from upstream to downstream. When particle collides with changing magnetic field associated with downstream plasma, it can reflect the particle back through the shock from downstream to upstream with increased velocity of v_1. In other words, this test particle effectively sees a plasma moving toward it with a speed of (v_{up} - v_{down}). If a similar process occurs in upstream side, then the particle will again increase its velocity to v_2. After the ith shock, the particle will have velocity v_i. So, $v_0 < v_1 < v_2 < ... < v_i$

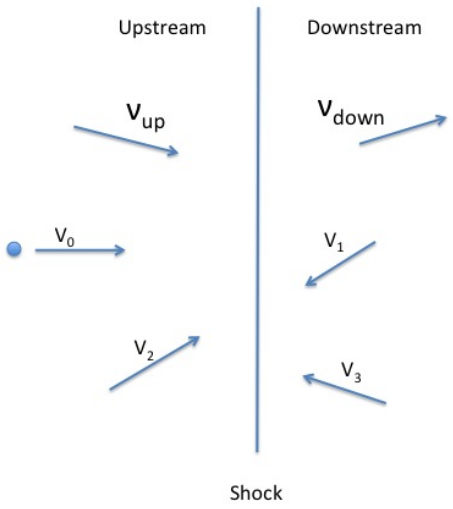

Figure 3.2. Shock Front.

Sequential diffusion back and forth causes increase in the speed of the particle and these multiple reflections hugely increase energy of the particles. So, the energy gain is always positive, and this mechanism naturally predicts a power-law distribution of particles. Assume that the shock is adiabatic and non-relativistic, radiative losses are unimportant, the gas around the shock is ideal, particles are relativistic, and

the unshocked gas material has Maxwell-Boltzmann distribution, then momentum of relativistic particle is [60],

$$p = \frac{E}{c}$$

After the first crossing, the particles will have the energy

$$E' = E + pv$$

For non-relativistic shock, the Lorentz factor is $\sim$1

$$\frac{\Delta E}{E} = \frac{v}{c}$$

So after j crossings, the energy is

$$E = E_0 B^j$$

and the particle distribution is

$$N = N_0 P_{shock}^j$$

where B = 1 + $\frac{v}{c}$ and P_{shock} is the probability of remaining in shock region. So,

$$\frac{N}{N_0} = (\frac{E}{E_0})^{\frac{logP}{logB}}$$

Finally, the particle distribution will be

$$n(E) \propto E^{\frac{logP}{logB}-1} = E^{-k}$$

where k = 1 - $\frac{logP}{logB}$, called power-law index.

3.2. Gamma Ray Emission Mechanism from SNRs

3.2.1. Leptonic Origin of Gamma Rays

If the particles gaining acceleration with Fermi mechanism are electrons then the gamma-ray production will be of leptonic origin. Electrons are charged leptons, which can interact with other particles. Same high energy electrons responsible for the synchrotron emission produce gamma rays via relativistic bremsstrahlung and inverse Compton processes.

3.2.1.1. Relativistic Bremsstrahlung. The process of producing photon is almost the same with thermal bremsstrahlung; due to Coulomb field of ions, electrons decelerate and emit photons by bremsstrahlung process, but in this case the electrons have relativistic energies. For the non-relativistic case, power per unit time, per unit volume and per unit frequency can be explained as [18],

$$\frac{dW}{dtdVdw} = \frac{16\pi^2 e^6 n_e n_i Z^2 g_{ff}(w,V)}{3\sqrt{3}c^3 m_e^2 v_e}$$

where n, w, n_i, Z, g_{ff}, e, c, m_e, v_e are electron density, the frequency, ion density, atomic number, Gaunt factor, charge unit, speed of light, mass of electron, and velocity of electron, respectively.

For the relativistic case,

$$dW' = \frac{dW}{\gamma}$$

where dW' is the emitted power per unit time and γ is the Lorentz factor,

$$\gamma = \frac{1}{1 - \sqrt{v^2 - c^2}}$$

So,

$$\frac{dW'}{dtdVdv} = \frac{16\pi^2 e^6 n_e n_i Z^2 g_{ff}(v,V)}{\gamma 3\sqrt{3} c^3 m_e^2 v_e}$$

3.2.1.2. Inverse Compton Process. When free electrons gaining energy from diffuse shock acceleration interact with low energy photons, they transfer some of their kinetic energies to lower-energy ambient photons. Sources of these soft photons could be interstellar radiation field, cosmic microwave background or far-infrared radiation by SNR itself. Lose rate in an inverse Compton process can be expressed as,

$$\frac{dE}{dt} = \frac{4}{3}\sigma_T c U_{rad} (\frac{v_e^2}{c^2})\gamma^2$$

where U_{rad}, σ_T, v_e, and γ and are energy the density of radiation in the rest frame of the electron, cross section, the velocity of the electron and the Lorentz factor.

3.2.2. Hadronic Origin of Gamma Rays

If the particles gaining acceleration with Fermi mechanism are protons, then the gamma ray production will be of hadronic origin. Interactions of accelerated protons with interstellar material produce neutral pions (π^0).

3.2.2.1. Production and Decay of Neutral Pions. The strong interaction of particles produces π^0 through the reaction: p+p $\rightarrow$ p+p+π^0. Energy conversations gives:

E= $2mc^2 = 2m_p c^2 + m_{\pi^0} c^2$ and $\gamma = \frac{1}{1-\sqrt{v^2-c^2}}$, $\gamma = \frac{m}{m_p}$

Where m, m_p, and m_{π^0} are mass of the incoming protons in the center of mass frame, mass of the proton and mass of π^0. The neutral pion mass is $\sim$135 MeV [17]. So, the two incoming protons must both be traveling at v=0.36c. This is the center of mass speed. Relative speed of the protons can be found with the Einstein velocity

addition

$$v_R = \frac{v_1 + v_2}{1 - \frac{v_1 . v_2}{c^2}}$$

gives v=0.64c.

Thus to create a π^0, it is necessary to give the incoming proton at least nearly 290 MeV of kinetic energy. π^0 is a kind of meson from the hadrons family, which consists of a quark and anti-quark, and it is an unstable particle. Gamma rays are emitted by the decay of π^0's produced in collisions between accelerated particles and the background gas in the following way [10].

(i) $\pi^0 \rightarrow \gamma + \gamma$ (with probability of 98%)
(ii) $\pi^0 \rightarrow e^- + e^+ + \gamma$ (with probability of 2%)

3.3. X-ray Emission Mechanism from SNRs

X-ray emission, from SNRs give information about interaction of swept-up ISM and ejected material and the plasma. The particles are considered 'ejected' if their kinetic energies are greater than their potential energies. Plasmas can be divided into two groups as optically thin and optically thick. If the plasma is optically thick, then the radiation generated is only moving a short distance within the medium and the spectrum is effectively blackbody dominated. If the plasma is optically thin, then the radiation generated is free to escape from the emitting region without interacting with the medium. The appropriate plasma emission model depends on both the temperature and the density. The plasma in SNRs are optically-thin, so the main observed emission processes are bremsstrahlung, and radiative recombination for continuum emissions, and line emissions. Also, synchrotron is contribution to the X-ray emission in SNRs as non-thermal emission. By analyzing observed continuum shape and line features of X-ray spectrum of SNRs, we can predict electron temperature (kT_e) and ionization temperature (kT_z) so that the ionization state of SNRs can be estimated.

3.3.1. Thermal Bremsstrahlung Emission

The most intense emission (in the order of keV) in a thin plasma is the bremsstrahlung emission, also called the free-free emission, because electron is free before and after the process. Due to Coulomb field of ions, electrons decelerate and emit photons by bremsstrahlung process. If we assume that plasma has low density and is collisionally ionized, electrons have the Maxwellian distribution, and external magnetic and electric fields are ignored. Then we can express emission power per unit time, per unit volume and per unit frequency as,

$$\frac{dW}{dtdVdw} = \frac{16\pi^2 e^6 n_e n_i Z^2 g_{ff}(v,V)}{3\sqrt{3}c^3 m_e^2 v_e}$$

where n_e, w, n_i, Z, g_{ff}, e, c, m_e, v_e are the electron density, the frequency, ion density, atomic number, Gaunt factor, charge unit, speed of light, mass of the electron and the velocity of the electron respectively. The Gaunt factor, g_{ff} is a function of energy of electron and frequency of emission. Shape and intensity of bremsstrahlung spectrum can give predictions about ion and electron densities and electron temperature.

3.3.2. Radiative Recombination

Radiative recombination (RRC) is also called free-bound emission in which an electron is captured by an ion and a photon is emitted. Electron is free before the process and bound after the process. The energy of produced photon is equal to binding energy of recombined electron and kinetic energy of electron. The energy of coming electron does not have a certain value so this process creates a continuous spectrum with a peak at the binding energy of the levels.

3.3.3. Line Emissions

This is a bound-bound transition between two discrete quantum levels. In this case, electron is bound before and after the process. Electron coming from a higher level to the lower level emits photon. Spectrum of line emissions shows a sharp edge

structure at the related energy levels. For a hydrogen (H) atom, the energy of an absorbed or emitted photon between two discrete levels is given by

$$E = R_y(\frac{1}{n^2} - \frac{1}{n'^2})$$

where R_y is Rydberg constant (=13.6eV) and n, n$'$ are principal quantum numbers of two discrete levels. We can generalize it for heavy elements, E roughly becomes

$$E = A^2 R_y(\frac{1}{n^2} - \frac{1}{n'^2})$$

where A is the atomic number of element. Line emissions in SNRs arise from H-like and He-like ions. For H-like ions, containing one electron, transitions between the states are referred as Lyα for 2p $\rightarrow$ 1s called Kα, Lβ for 3p $\rightarrow$1s called Kβ and Lyγ for 4p $\rightarrow$1s called Kγ. Line energies of Lyman series for the elements mostly seen is given in Table 3.1 in eV.

Table 3.1. H-like emission lines energies of some elements mostly observed in SNRs in eV [44].

	Lyα	**Lyβ**	**Lyγ**
Mg	1472	1745	1840
S	2006	2377	2506
Si	2623	3107	3277
Ar	3323	3936	4151
Ca	4106	4864	5130
Fe	6966	8266	8732

He-like ions produce three intense lines. There are three transition lines for Heα, resonance (1s2p $^1P_1 \rightarrow 1s^2\ 1S_0$) forbidden (1s2s $3S^1 \rightarrow 1s^2\ 1S_0$) and intercombination (1s2p $3^1P_{1,2} \rightarrow 1s^2\ 1S_0$). Line energies of He-like transition of elements for Heα emission is given in Table 3.2 in eV.

Table 3.2. He-like emission lines energies for Heα transitions of some elements mostly observed in SNRs in eV [44].

	Resonance	**Forbidden**	**Intercombination**
Mg	1352	1330	1340
S	1865	1840	1854
Si	3140	3104	3124
Ar	3908	3845	3892
Fe	6702	6641	6670

The Heβ and Heγ transition lines energies in eV for the elements are given in Table 3.3.

Table 3.3. He-like emission lines energies for Heβ and Heγ transitions of some elements mostly observed in SNRsin eV [44].

	Heβ	**Heγ**
Mg	1579	1660
S	2183	2294
Si	2884	3033
Ar	3685	3875
Ca	4582	4819
Fe	7798	8217

3.3.4. Synchrotron Radiation

When charged particles are accelerated in a magnetic field, they emit radiation throughout a gyrating path, which dominates much of high-energy emission generated in SNRs. For non-relativistic particles, the radiation is simpler and called cyclotron radiation. However, extremely relativistic particles have a much more complex frequency spectrum extending to the gyration frequency [14], known as synchrotron radiation.

Figure 3.3 shows the path that the electrons follow in strong magnetic field [14].

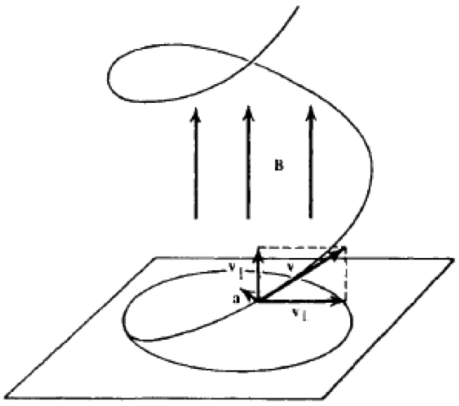

Figure 3.3. Helical motion of an electron in uniform magnetic field.

Total emission power for an accelerated electron is,

$$P_{syn} = \frac{4}{3}\sigma_T c\beta^2\gamma^2 U_B$$

where

$$\sigma_T = \frac{8}{3}\frac{\pi r_0^2}{\beta}$$

and

$$U_B = \frac{B^2}{8\pi}$$

where σ_T, U_B, c, v, r_0 are cross section, magnetic energy density, speed of light, velocity of the electron, and the radius of the helical path, respectively.

3.3.5. Thin Thermal Plasma in SNRs

Thin thermal plasmas have the characteristics of high temperature ($\sim 10^6$-10^8 K) and low density (~ 1 cm^{-3}) mostly seen in SNRs. X-ray investigation of SNRs gives information about ionization states of plasmas, because such high temperature plasmas are dominated by X-ray emission. Studying the ionization states of plasmas enables us to estimate the evolutionary states of SNRs. For optically thin thermal plasmas, it takes a time of 10^4-10^5 years to reach collisional ionization equilibrium (CIE) with electrons heated by shock wave. Classification of thin thermal plasmas depends on ionization balance. Here we will introduce three kinds of plasmas with respect to their balances of ionization and electron temperatures. Those are ionizing, equilibrium and recombining plasmas showing different spectral features. In this thesis, we assumed Maxwell-Boltzmann distribution of electrons in thin thermal plasmas [15].

$$f(v) = 4\pi v^2 (\frac{m}{2\pi k T_e}) \exp(\frac{-mv^2}{2kT_e})$$

Competition of ionization and recombination processes determines the states of plasmas. There are three ionization processes: collisional ionization, photoelectric ionization, and auto-ionization. Also three inverse processes: 3-body recombination, radiative recombination and dielectronic recombination form recombination side.

3.3.5.1. Ionizing Plasma ($kTe > kTz$). This is called underionized stage. In this state, atoms are less ionized. Electron temperature (kT_e) is larger than ionization temperature (kT_e), so ionization dominates recombination. This state is observed in young SNRs such as Cas A and Tycho.

3.3.5.2. Equilibrium Plasma (kTe = kTz). This stage is called ionization equilibrium. A balance between ionization rate and recombination rate is achieved. In this state, ionization mostly occurs by electron collisions.

3.3.5.3. Recombining Plasma ($kTe < kTz$). In this state, atoms are highly ionized. It is called overionized state. Electron temperature (kT_e) is smaller than ionization temperature (kT_z) so recombination rate exceeds ionization rate.

4. INSTRUMENTS

4.1. Fermi Gamma Ray Space Telescope

4.1.1. Overview and Mission

Fermi Gamma Ray Space Telescope (Fermi) was launched in 11 June 2008 from Cape Canaveral Air Force Station, Florida. The design life of the mission is expected to be 5 years and the goal for mission operations is 10 years. Fermi has energy range from 20 MeV to 300 GeV. It covers the whole sky every 3 hours by orbiting at an altitude of 550 km and at an inclination of 28.5^o. Fermi project is collaboration of more than 400 scientists from 90 universities in 12 countries. It is funded by National Aeronautics and Space Administration (NASA) from USA, Centre National de la Recherche Scientifique (CNRS) from France, Istituto Nazionale di Astrofisica from Italy, Aerospace Exploration Agency from Japan and National Space Board from Sweden.

Fermi has the following scientific objectives [21];

- Determining the nature of the unidentified sources and the origins of the diffuse emission revealed by EGRET.
- Understanding the mechanisms of particle acceleration operating in celestial sources, particularly in active galactic nuclei, pulsars, supernovae remnants, and the Sun.
- Understanding the high energy behavior of GRBs and transients.
- Using gamma-ray observations as a probe of dark matter.
- Using high-energy gamma-rays to probe the early universe and the cosmic evolution of high-energy sources.

Figure 4.1 shows all gamma rays that Fermi has observed during its 3 years mission. Color scale shows number of photons with energy greater than 1 GeV detected per pixel in the first 2 years of Fermi operation. Fermi consists of two main parts, which

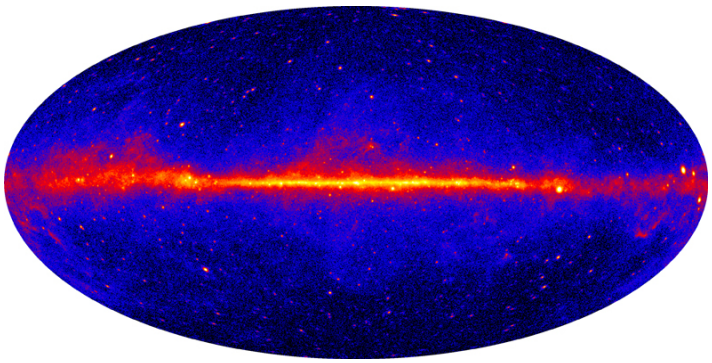

Figure 4.1. GeV gamma-ray sky. Color scale shows number of photons with energy greater than 1 GeV detected per pixel in the first 2 years of LAT operation.

are Large Area Telescope and Gamma-ray Burst Monitor [21].

4.1.2. Large Area Telescope - LAT

The Large Area Telescope (LAT) is the main scientific instrument on the Fermi spacecraft. It was originally called Gamma-Ray Large Area Space Telescope (GLAST). The LAT is an imaging telescope having wide field-of-view to detect high-energy gamma-ray events. The LAT can measure the directions, energies and arrival times of incident gamma rays with its large field of view, also can reject background from cosmic rays. The LAT has many higher scientific and technical features from other gamma-ray space telescope experiments. Energetic Gamma Ray Experiment Telescope (EGRET) was the previous gamma-ray mission. Table 4.1 shows the differences of these two experiments and basic properties of LAT. The LAT was built at Stanford University. It consists of 4x4 totally 16 array of identical towers, each having 40×40 cm^2 area. The LAT has 4 parts working collaboratively with each other.

4.1.2.1. The Anti-Coincidence Detector - ACD. It is the first defense against charged cosmic rays located around the tracker to reject cosmic background events. ACD is one layer structure and its total thickness is 10 mm. ACD has high detection efficiency for charged particles (> 0.9997) [21]. When charged particles hit plastic tiles on ACD,

Table 4.1. LAT comparison with previous experiments.

	LAT	**EGRET**
Energy Range	20 MeV - 300 GeV	20 MeV - 30 GeV
Peak Effective Area	< 8000 cm^2	1500 cm^2
Field of View	< 2 sr (steradian)	0.5 sr
Angular Resolution	$< 3.5^0$ for 100 MeV	$< 5.8^0$ for 100 MeV
Energy Resolution	$< 10\%$	10%
Deadtime per Event	100 μs	100 ms
Source Location Determination	> 0.5'	10'
Point Source Sensitivity	$< 6\times10^{-9}$ cm^{-2} s^{-1}	$\sim10^{-7}$ cm^{-2} s^{-1}

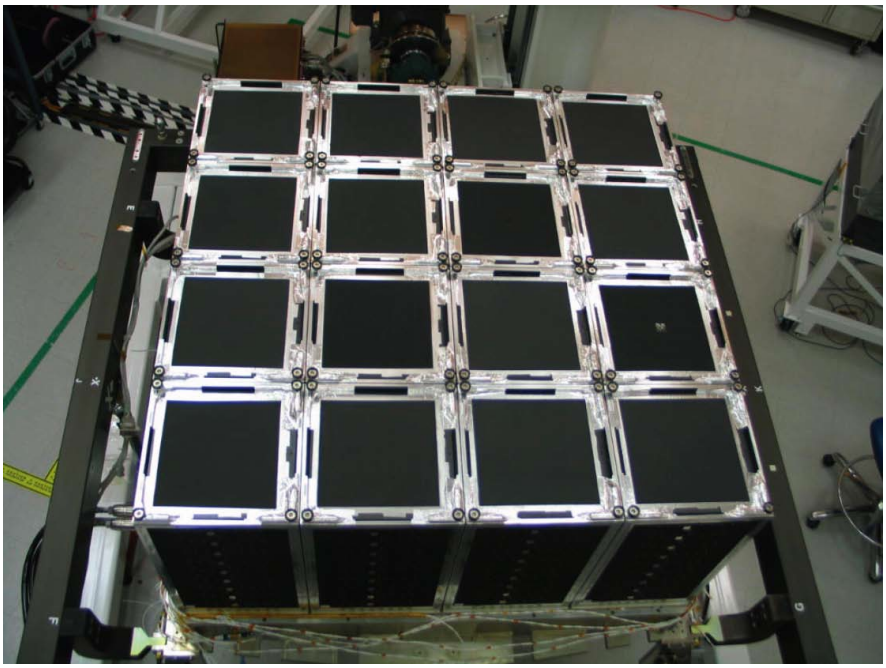

Figure 4.2. Fermi LAT design. Figure is taken from Atwood *et al.* [21].

Table 4.2. Sources of Fermi 2nd year catalog results [22].

	Identified #	**Associated #**
Pulsar, identified by pulsations	83	...
Pulsar, no pulsations seen in LAT yet	...	...
Pulsar Wind Nebula	3	...
Supernova Remnant	6	4
Supernova Remnant / Pulsar Wind Nebula	...	58
Globular Cluster	...	11
High Mass Binary	4	...
BL Lac Type of Blazar	1	...
FSRQ Type of Blazar	7	429
Non-Blazar active galaxy	17	10
Radio Galaxy	2	10
Seyfert Galaxy	1	5
Active Galaxy of Uncertain Type	0	257
Normal Galaxy	2	4
Starburst Galaxy	...	4
Uncertain Class	...	1
Unassociated	...	575
Total	127	1746

they produce flashes of light. However, when gamma rays are electromagnetic waves, they do not produce flashes. 5×5 array plastic scillinator tiles forward the light to photomultiplier tubes via wavelenght shifting fibers.

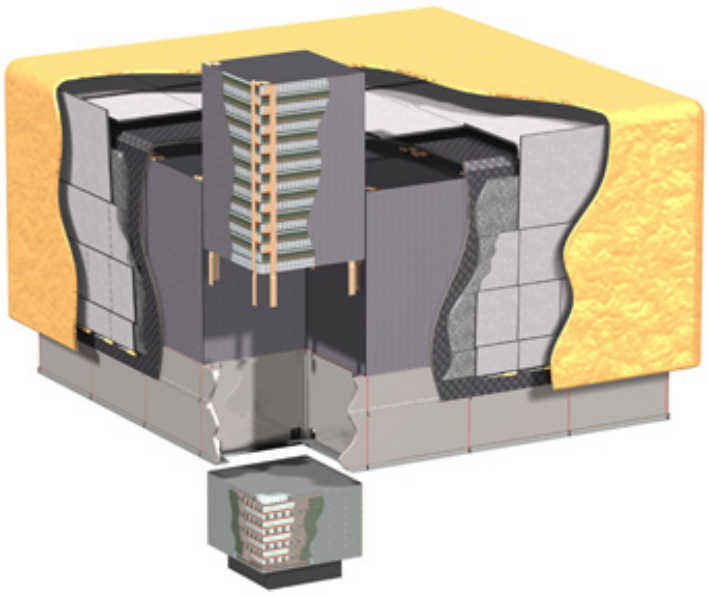

Figure 4.3. LAT schematic view. Yellow layers show ACD. The figure is taken from Atwood *et al.* [21].

4.1.2.2. The Tracker. The tracker has two main functions. First one is to convert the incident gamma-ray to electron positron pairs with tungsten foil layer modules. There are 12 thin layers with 0.03 radiation length at the front and 4 thick layers with 0.18 radiation length at the back of the tracker. Tungsten layers are high-Z materials. The other function is to precisely measure the paths of the electron and positron produced from the initial gamma-ray. The silicon strip layers are used for the path measurement. Planes of the silicon detectors are orthogonally arranged so that the x,y, and z-directions can be determined.

4.1.2.3. The Calorimeter. Calorimeter measures the energy of electron and positron after they are totally absorbed. It is made of cesium iodide CsI. It also helps to reject cosmic rays, since their pattern of energy deposition is different from that of gamma

rays.

4.1.2.4. Data Acquisition System. This system is the brain of LAT. This part collects information from tracker (silicon strip detectors) and calorimeter, and provides an on-board event science analysis platform.

4.1.3. Gamma-ray Burst Monitor - GBM

Gamma-ray burst monitor consists of 14 detectors and a data processing unit. There are 12 low-energy detectors made of sodium iodide responsible for the events from 8 keV to 1 MeV. Also there are 2 high-energy detectors made of bismuth germanate responsible for the events from 150 keV to about 30 MeV.

4.1.3.1. Low Energy Detectors. Each low energy detectors are 12.7 cm in diameter. They are mounted in 4 groups consisting of 3 detectors oriented in various directions so that they face different parts of the sky. They provide the locations of gamma-ray bursts to within several degrees.

4.1.3.2. High Energy Detectors. High energy detectors are positioned on opposite sides of the spacecraft, providing nearly full sky coverage. They are made of bismuth germanate (BGO), which is a high density material. They provide a good overlap with low energy range of LAT.

4.1.3.3. Data Processing Unit. The signals from all 14 GBM detectors are collected by a central data processing unit. It has 3 main missions,

- Identifies GRBs, determines their energies and arrival directions.
- Digitizes and time-tags the detectors, pulse height signals, and packages the resulting data into several different types for transmission.
- Directs the data to the Fermi spacecraft's transmission unit to be sent the ground.

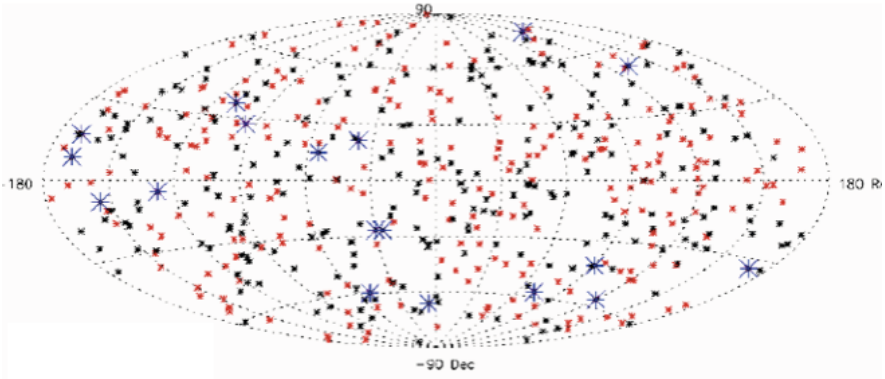

Figure 4.4. Gamma-ray Bburst sky. 264 GRBs (in red) in the field of view of LAT out of total 514. GRB2010 conference results Annapolis, 2010.

4.2. Chandra X-ray Observatory

The Chandra X-ray Observatory (CXO) was launched on July 23 1999 from Columbia Space Shuttle. Main mission of Chandra is to observe X-rays from high-energy regions of the universe. CXO has an elliptical orbit with apogee height of 120.300 km and perigee height of 28.600 km and the period is 63.5 hours yielding high observing efficiency. Chandra consists of 3 main parts; the X-ray telescope, the science instruments and the spacecraft.

4.2.1. X-ray Telescope

Chandra telescope system has the principal elements, the High- Resolution Mirror Assembly (HRMA) having 4 mirrors. These concentric paraboloid-hyperboloid grazing incidence X-ray mirrors have focal lenghts of 10 m, and the diameters of 1.2 m. Figure 4.5 gives a general look to CXO [20].

4.2.2. The Science Instruments

The Chandra X-Ray Observatory combines the mirrors with 4 science instruments: 2 main instruments are ACIS and HRC designed to provide information about

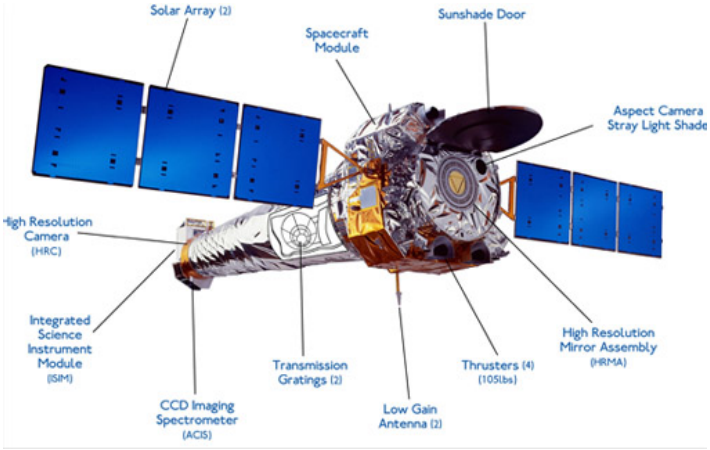

Figure 4.5. Chandra X-ray Observatory view.

direction, energy and arrival times of incoming photons. 2 additional science instruments; The Low Energy Transmission Grating LETG and The High Energy Transmission Grating - HETG spectrometers provide detailed information about X-ray energy.

4.2.2.1. Advanced CCD Imaging Spectrometer - ACIS. The ACIS consists of ten 1024 ×1024 pixel CCDs (Charge Coupled Device). CCDs, made of silicon, are solid state electronic devices. These 10 CCDs are arranged in two arrays. Pixel size of ACIS is 0.4920" ± 0.0001". So, ACIS-I has 2×2 CCDs, 16.9'×16.9' array size, and ACIS-S has 1×6 CCDs and array size of 8.3'×50.6' [19]. Figure 4.6 shows chip design of ACIS in CXO [53].

Two of the CCDs are back-illuminated (BI) and eight of the CCDs are front-illuminated (FI). S1 and S3 chips are back-illuminated because their back sides faces the incoming X-rays. ACIS detector operator temperature is changing between -90 ^0C and -120 ^0C. The spatial resolution of imaging with ACIS is limited with physical size of the CCD pixels (0.492"). The spectral resolution depends on measuring the total charge by a photon. The fraction of the charge collected, the fraction of the charge lost during read-out in transfer and the ability of the read-out amplifiers to measure the charge are used to determine total charge by a photon in the ACIS system. Highest resolution is obtained within 1'-2' depending on the energy of the source. The Time

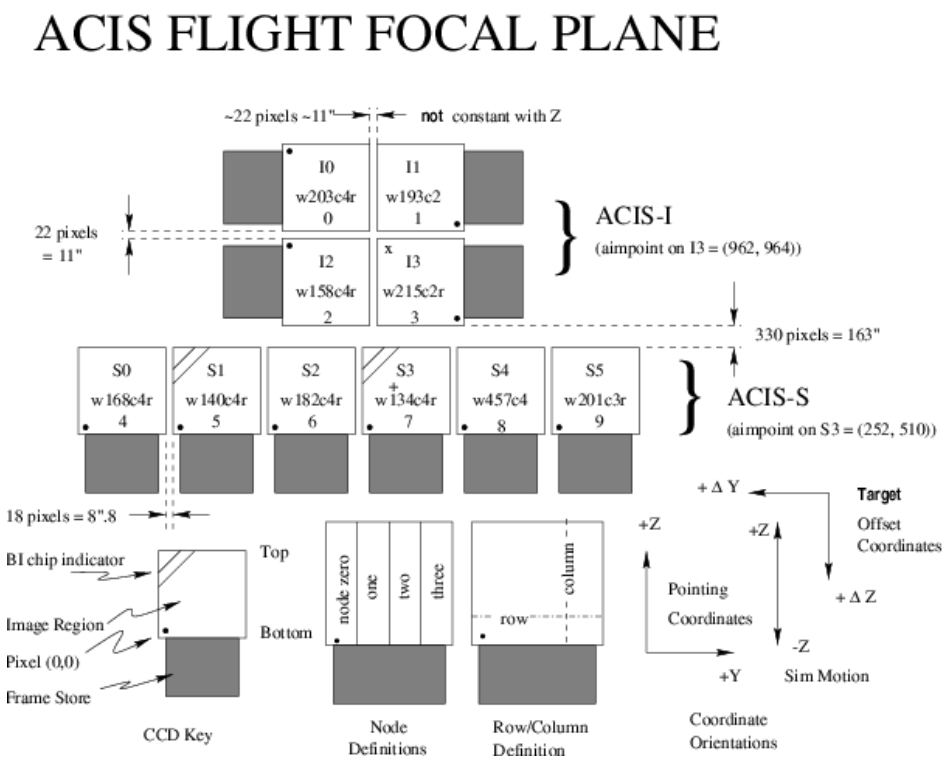

Figure 4.6. ACIS CCD design.

Exposure Mode defined as the mode where the selected region is exposed for a fixed amount of time. The observations used in this thesis were obtained in this mode.

4.2.2.2. High Resolution Camera -HRC. The HRC has 2 microchannel plate (MCP) detectors; HRC-S and HRC-I which are optimized for imaging. The HRC-I is capable to give response to events having energies 0.8 - 10 keV and has a field of view of $\sim$ 30'×30' and pixel size of 0.13". When X rays enter to the HRC, UV/Ion shield reduces the signals from UV light, ions, and low energy electrons absorbed in the Csl-coated walls. The resulting photoelectrons are accelerated by an external electric field and forming signals.

4.2.2.3. HETG and LETG Spectrometers. Main missions of HETG and LETG is to diffract the intercepted X-rays, changing their direction, which depends on the energy of incoming X-ray. LETG is a gold grating, made of fine wires, having a period or

regular spacing of 1 μm. LETG is designed to cover an energy range of 0.08 to 2 keV. HETG has regular spacing of 0.2 1μm or 2000$\mathring{A}$ for the high-energy gratings, and 0.4 μm or 4000$\mathring{A}$ for the medium energy gratings. The HETG is designed to cover an energy range of 0.4 to 10 keV. Figure 4.7 indicates HRC design [55].

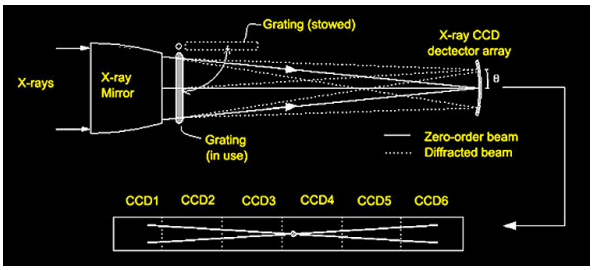

Figure 4.7. Schematic view of grating spectrometers.

4.2.3. Spacecraft

In order to work efficiently, the telescope and the science instruments need the supportive structure. The spacecraft provides necessary environment for them. Motion, heat, and energy are essential for an observatory. For the motion, Chandra has two different thrusters: one is for propulsion and the other one is for momentum unloading. Chandra's thermal control system, cooling radiator, insulators, heaters, and thermostats controls the temperatures of critical components. The energy stored in three banks of batteries of Chandra provides electrical power comes from its solar arrays.

5. ANALYSIS & RESULTS

5.1. CASSIOPEIA A

5.1.1. Overview of the Previous Results of Cas A

Cassiopeia A (Cas A) is one of the youngest supernova remnants, thought to be the result of either a Type Ib or Type IIn supernova explosion occurring in 1671 [36]. Angular size of 2.5' in radius, corresponding physical size is 2.34 pc and at the distance 3.4 kpc [24]. Cas A has shock speed of 5200 km/s and age of nearly 320 yr [25]. It is a shell type supernova remnant. The detection of non-thermal emission from radio observations reveals that Cas A is a bright radio source [7]. Akari and Blast observations of Cas A reveals a new tepid dust grain population at a temperature of $\sim$ 35 K and with an estimated mass of 0.06 solar mass [26]. Supernova light echo (LE) spectra of Cas A have been recently detected by Rest A. [27]. Cas A is viewed in X-rays, the remnant consists of a line emitting shell arising from reverse shocked ejecta rich in O, Si, Ar, Ca, and Fe [28], [50]. Chandra X-ray observatory revealed detailed image of Cas A having thin structures near the forward shock [31]. For Cas A, non-thermal emission filaments are associated with the forward shock however non-thermal X-ray emission is also seen in projection in the interior of the SNR [32]. It is still uncertain whether these interior filaments arise from the forward shock seen in projection or originate from non-thermal emission mechanisms in the interior of the SNR [34]. Cas A was observed in GeV too. Fermi detection of Cas A announced in 2010 with a significance of 12.2σ and the integral photon flux above 500 MeV of $(8.7 \pm 1.3) \times 10^{-9}$ photons $\mathrm{cm}^{-2}\mathrm{s}^{-1}$ [57]. Fermi collaboration has claimed that magnetic field strength with 0.3 mG best predicts gamma-ray flux. First TeV emission has been detected by HEGRA (High Energy Gamma-Ray Astronomy experiment) collaboration [33]. VERITAS (The Very Energetic Radiation Imaging Telescope Array System) observations have given estimation of integral flux for this gamma-ray source is about 3% of the Crab-Nebula flux above 200 GeV [58].

5.1.2. Fermi-LAT Analysis of Cas A

Fermi observation of Cas A between the dates 08.04.2008 and 01.30.2012 was used in the analysis. Total exposure time was nearly 34 months. 9 photon database (PH) and a specraft pointing including livetime and history database (SC) files were handled. The LAT data was extracted at the point of right ascension (RA) : 350.85^o and declination (Dec) : 58.81^o. The LAT data in the region of 20^o and in the energy range of 200 MeV - 300 GeV was required from Fermi Science Support Center (FSSC's) web site data server.

5.1.2.1. Data Preparation. The events which are not within the extraction region used for the analysis were filtered out by *gtselect* tool. The radius of new search region was selected as 12 degrees. Lower energy limit of 500 MeV and upper energy limit of 50 GeV were used, because the source was detected only above 500 MeV and significant emission could not be found above 50 GeV. Photons coming from the zenith angle larger than 105^o were rejected to reduce the background from gamma rays produced in the atmosphere of the Earth. The *gtmktime* tool provides an opportunity to select good time intervals (GTIs) by filtering on information provided in the spacecraft file. Some spacecraft events can negatively affect the quality of the data, this tool excludes time periods related with these events and ensures the LAT instrument was in normal science data-taking mode. Also rock angle of 52^o (recommended by the LAT team) was used to eliminate pointed observations from the dataset.

5.1.2.2. Creating Count Cube and Map. The count cube of the region of interest was created by CCUBE option of *gtbin* tool. Size of the X and Y axis in pixels was selected to be both 80, image scale was 0.1^o/pixel and 8 number of logarithmically uniform energy bins were used. This count cube is also used in source map analysis. Figure 5.1 shows counts map of Cas A smoothed with 3σ in the range of 0.2 - 300 GeV. Counts map was viewed using the tool *ds9*.

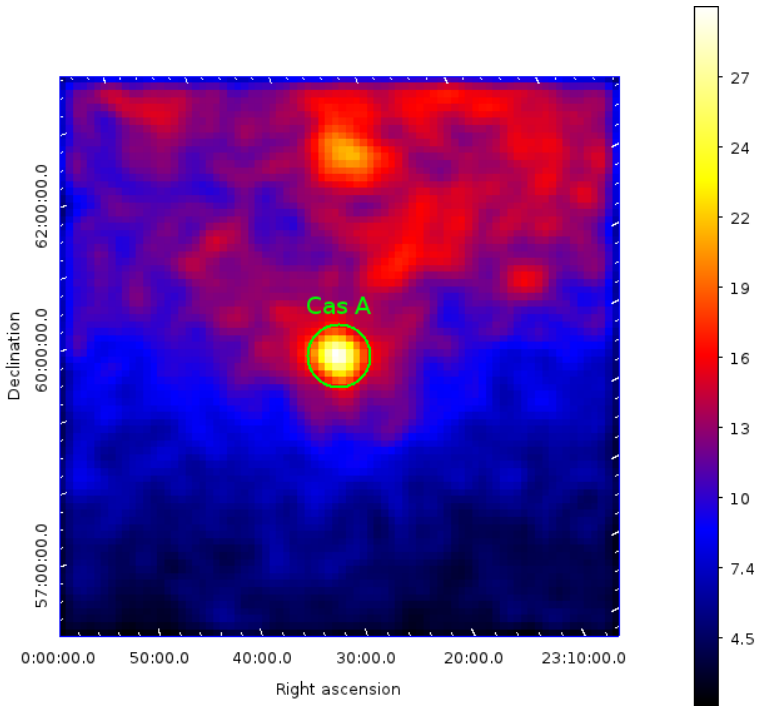

Figure 5.1. Cas A counts map smoothed with 3σ and in the energy range of 0.2-300 GeV.

5.1.2.3. Building Background Model. The *gtlike* tool reads the source model from a XML file. We have created the XML file including all the background sources using Fermi 1st year catalog. The sources having the distance smaller than $\sim 10^o$ and having significance bigger than 5σ were selected. Background model consists of 10 point sources chosen within the analysis region. Also galactic diffuse component (*gal_v02*)and isotropic extragalactic emission(*eg_v02*) were added to the model. Table 5.1 shows the distances and the significances of the background sources in the analysis region.

5.1.2.4. Computing Exposures and Source Map. In order to exposure of the source, we need to calculate livetime of the observation. *gtltcube* tool was used to calculate how much time the LAT has observed given position on the sky at given inclination angle. This tool calculates the time range covered by the spacecraft file. Exposure map of Cas A was performed by *gtexpcube2* tool. Size of the X and Y axis in pixels was selected to be again 400, image scale was 0.1 degree/pixel and 8 bins were used in the energy range of 500 MeV to 50 GeV. The exposure map was performed using the LAT Science

Table 5.1. Background point sources located within the radius of 10^o around the location of Cas A.

	Distance to ROI Center (degree)	**Significance (σ)**
1FGLJ2238.4+5903	5.79	21.06
1FGLJ0000.8+6600c	8.37	9.84
1FGLJ0003.1+6227	6.07	7.79
1FGLJ2214.5+5949	8.81	5.83
1FGLJ2229.0+6114	7.18	56.23
1FGLJ2250.8+6336	6.18	6.66
1FGLJ2347.1+5142	7.86	10.58
1FGLJ0009.1+5031	7.86	10.58
1FGLJ0035.9+5951	9.27	13.01
1FGLJ0038.6+6306	10.04	5.15

Tools package with the P6_V11_DIFFUSE post-launch instrument response function. The source map was computed by *gtsrcmaps* tool. The tool takes each source spectrum in our XML model, multiplies them by their related exposures at the source positions, and convolves that exposure with the effective point spread function (PSF). Response function of P6_V11_DIFFUSE, exposure map and count cube created were used in the source map.

5.1.2.5. Binned Likelihood Analysis of Cas A. For the most of the LAT analysis, binned likelihood analysis is used. Unbinned likelihood analysis is generally recommended for the data having periodical short time observations. The likelihood L can be best described as the probability of obtaining the data for a given input model [49]. In Fermi analysis, the input model is the distribution of gamma ray sources on the sky, and includes their intensity and spectra and the data is the list of counts produced by LAT. To analyze LAT data, we construct the likelihood that is applicable to LAT data, and then use this likelihood to find the best fit model parameters.

5.1.2.6. Fermi Analysis Results of Cas A. After producing exposure, count and source maps, and the background model *bdlike* script was run to create count spectrum, TS vs energy and dN/dE vs energy spectrums. Fermi analysis clearly showed the source at a reasonable level. The source was detected at a significance level 26σ (TS value of 676). Cas A was fitted with power law and integral photon flux obtained was (17.6 $\pm$ 0.11)$\times 10^{-9}$ photons cm^{-2}s^{-1}. Spectral index was found to be $\Gamma = 2.02 \pm 0.04_{stat}$. Figures 5.2, 5.3, and 5.4 show TS vs energy, flux vs energy, and count spectrums, respectively.

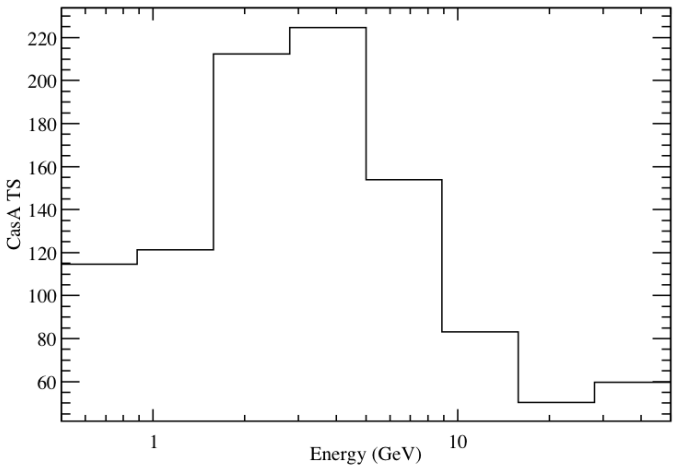

Figure 5.2. Fermi gamma-ray energy spectrum of Cas A.

5.1.3. Chandra X-ray Analysis of Cas A

Chandra 1 Ms observation of Cas A was taken with S3 CCD chip (chip no: 7) of Advanced CCD Imaging Spectrometer (ACIS) was used. The observation, having obs-id of 4638, was performed in April 2004. Exposure time was given as 166720 s to the point RA: 23h 23' 26".70 DEC: +58^o 49' 03".0 [50]. Cas A was observed in graded datamode and timed readmode.

5.1.3.1. Data Reduction. To analyze the data, CIAO 4.4 version of Chandra Calibration Data Base, released in 15 December 2011, was used. Main purpose of the data

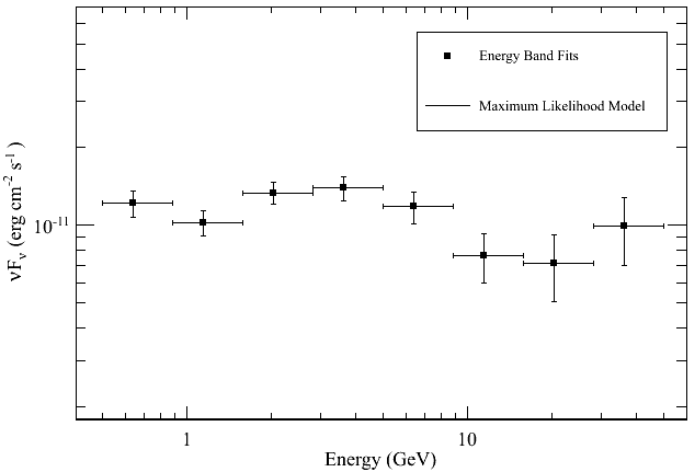

Figure 5.3. Fermi gamma-ray Flux vs Energy spectrum of Cas A.

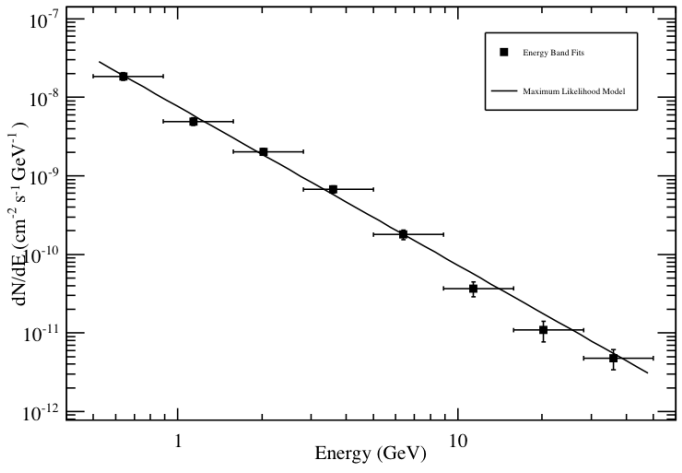

Figure 5.4. Fermi gamma-ray Count Spectrum of Cas A.

reduction is to generate a new event 2 file on which afterglow effects and charge transfer inefficiency are corrected, bad-pixels are removed, and filtering on grade, status and good time were made. In order to make the necessary reductions on the Cas A data, CIAO 4.4 science threads were followed.

(i) *Reproducing Chandra Data*: The script *chandra_repro* reproduces the observation data downloaded from HEASARC (The High Energy Astrophysics Science Archive Research Center). This scripts generates a new bad pixel file, a new level=2 event file, and a new level=2 Type II PHA (Pulse Height Analyzer) file and also includes grade and status filtering changes.

(ii) *Removing Destreak Events*: Due to extreme conditions in the environment of Chandra X-ray Observatory, the front illuminated CCDs in the ACIS were damaged early in the Chandra mission. Enhanced charge transfer inefficiency (CTI) during parallel readout causes loss of charge in the CCD as data transferred among the pixels. This causes spatial redistribution of charge and decrease in energy resolution. Effects in observed spectral distribution arise from changing pulse height distribution, so this produces a gain shift. So *acis_process_events* script has corrected this inefficiency in charge transfer. Also, in order to improve the streak detection efficiency and to prevent pixels with several streak events from being misidentified as hot pixels, *destreak* tool is performed. Before generating a new bad pixel file, removing the streaks develops the streak detection efficiency and prevents misidentifying pixels with many streak events as hot pixels. So, running *destreak* can improve the quality of the data.

(iii) *Checking Observation Mode and Clearing the Status*: There could be 2 observational mode options for the Chandra data. If the data is in TIMED mode, you should make a new bad-pixel file. However if it is CC-mode data, you should make a new level=1 event file by *acis_process_events* script.

(iv) *Creating a New Bad Pixel File*: Each Chandra observation has specific bad pixels. These bad pixels generally are hot pixels producing high or saturated pulse heights. During the observation, photons falling on these bad pixels are excluded from analysis. Extraction of bad pixel was performed with the tool *acis_process_events*. We created a new bad pixel file for the event 2 file that we

will generate.

There are 4 steps to do that,

- Generating *obs.par* file for the observation
- Identifying bad pixels and columns from the calibration database and pixels with bad bias values
- Searching for afterglows and hot pixels
- Marking pixels adjacent to afterglows and hot pixels and sort the list of bad pixels and afterglows

(v) *Generating a New Level-1 File*: First we should look at the readmode and datamode of the data to decide what the event definition is. We used graded datamode and timed readmode data. So, our eventdef was chosen as grdlev1. So running *acis_process_events* with the event definition produces a new level 1 file.

(vi) *Filtering on Grade, Status, and Good Time*: Our observation was imaging data, so that there were two filtering steps for ACIS imaging observations

- Filtering for bad grades and for a "clean" status column
- The Good Time Intervals (GTIs) supplied by the pipeline and are stored in the event1 file. Simultaneously, unnecessary columns are eliminated from the output

So, *acis_repro_evt2.fits* is a level=2 event file with the latest calibration products is created.

(vii) *Applying Energy Cut*: We applied energy cut to *evt2* file, we have chosen the option copying all blocks in the input file, not just the one you are filtering. The other blocks were copied without change. The energy range from 0.3 to10 keV was selected from the data.

5.1.3.2. Image Analysis of Cas A. The images of Cas A in different energy bands were obtained. *dmcopy* tool was used creating image files and *ds9* tool was used to view the images. 4 images were created using Cas A chandra data after the data reduction. Cas A image in the range of 0.3 - 8 keV can be seen in Figure 5.8. Figures from 5.5 to 5.7 show soft energy (0.3 - 1.5 keV), medium energy (1.5 - 2.5 keV), and hard energy (2.5 - 8 keV) images of Cas A, respectively. Also, a combined image of soft, medium,

and hard energies was produced using *ds9* tool, and can be seen in Figure 5.9.

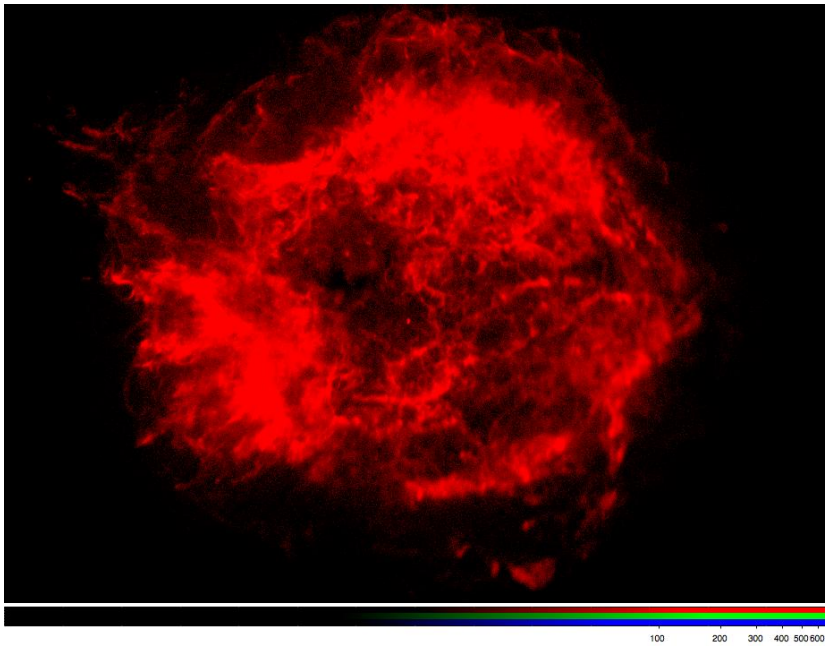

Figure 5.5. Cas A Chandra soft energy X-ray image in the range of 0.3 - 1.5 keV.

5.1.3.3. Spectral Analysis of Cas A.

(i) *Producing Count and Response Files*: First step of creating the spectra is to select regions of interest. We have selected 5 regions dominantly observed in 2.5-8 keV image using *ds9* to be analyzed because we are interested in radiation due to non-thermal synchrotron emission. Synchrotron emission produces hard X-ray photons in SNRs. Those regions has been chosen from the shell of the remnant where non-thermal X-ray emission is observed in thin filaments associated with the forward shock. Figure 5.10 shows selected region for spectral analysis on the combined image of Cas A. Four files have been created to extract the spectrums,

- The files of the photon counts for selected regions were generated using *dmextract* tool of The CIAO Data Model. The function of *dmextract* is to create a histogram from a column of data in a table.
- The file of the photon counts for background region was generated using *dmextract* tool of the CIAO data model.

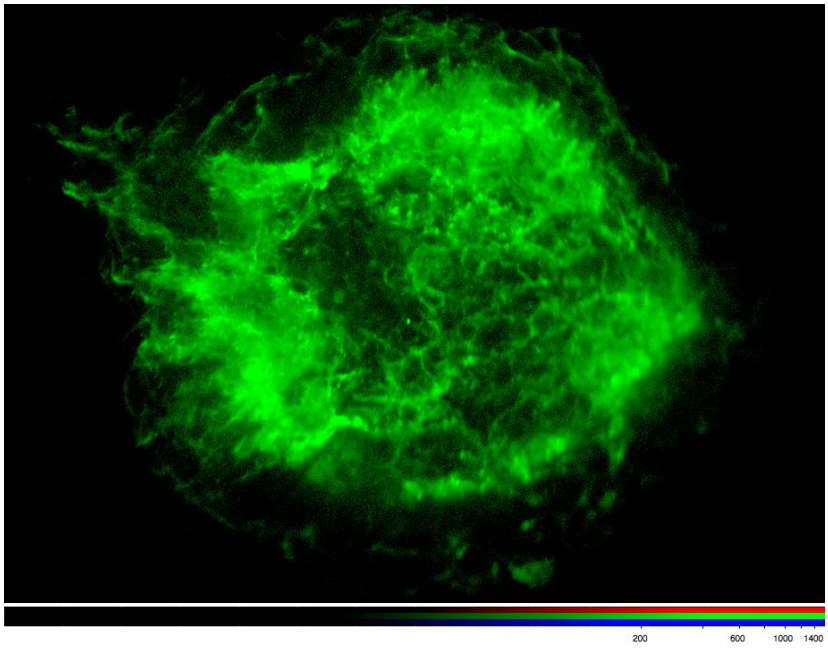

Figure 5.6. Cas A Chandra medium energy X-ray image in the range of 1.5 - 2.5 keV.

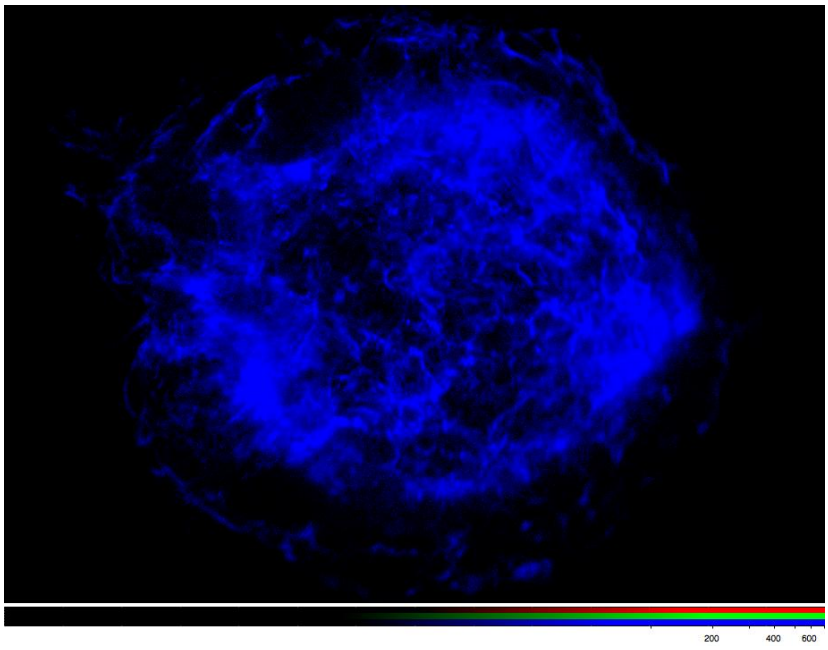

Figure 5.7. Cas A Chandra hard energy X-ray image in the range of 2.5 - 8.0 keV.

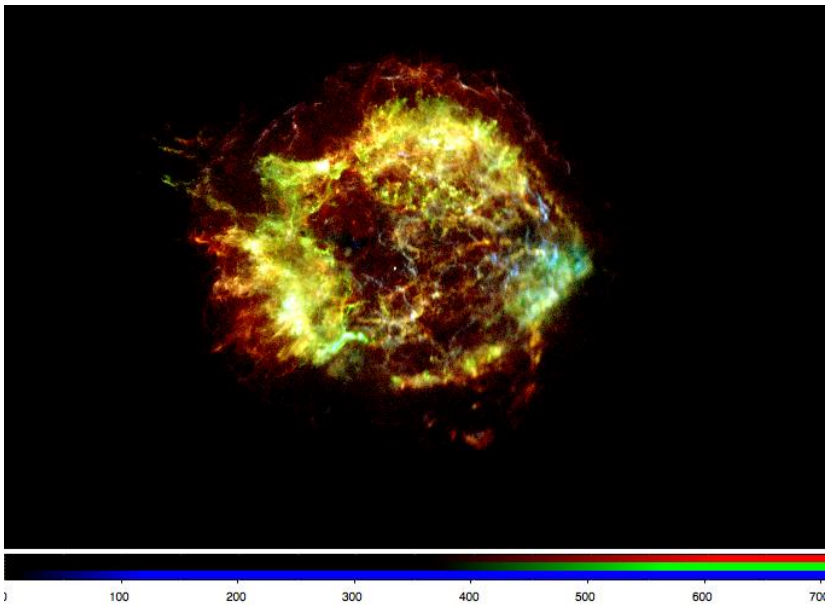

Figure 5.8. Cas A Chandra image in the range of 0.3 - 8 keV.

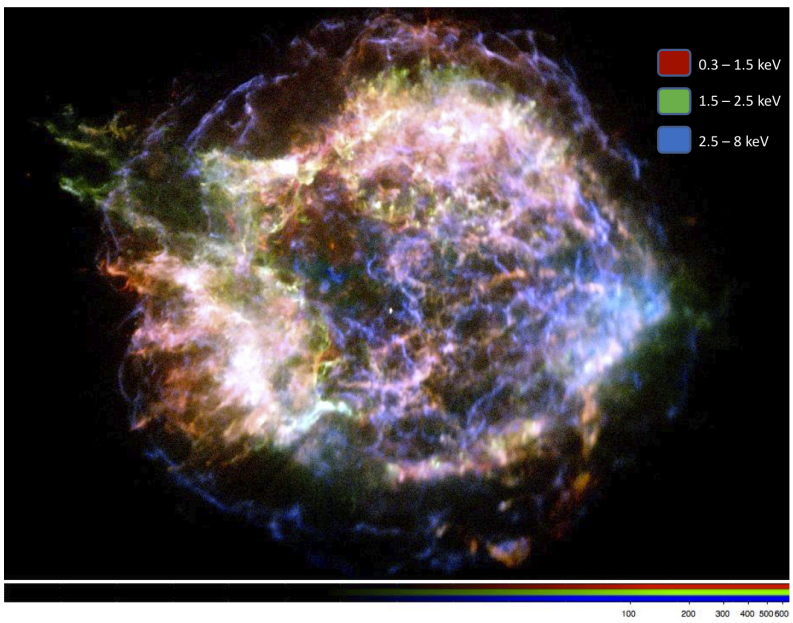

Figure 5.9. Cas A Chandra combined image of soft, medium and hard energies.

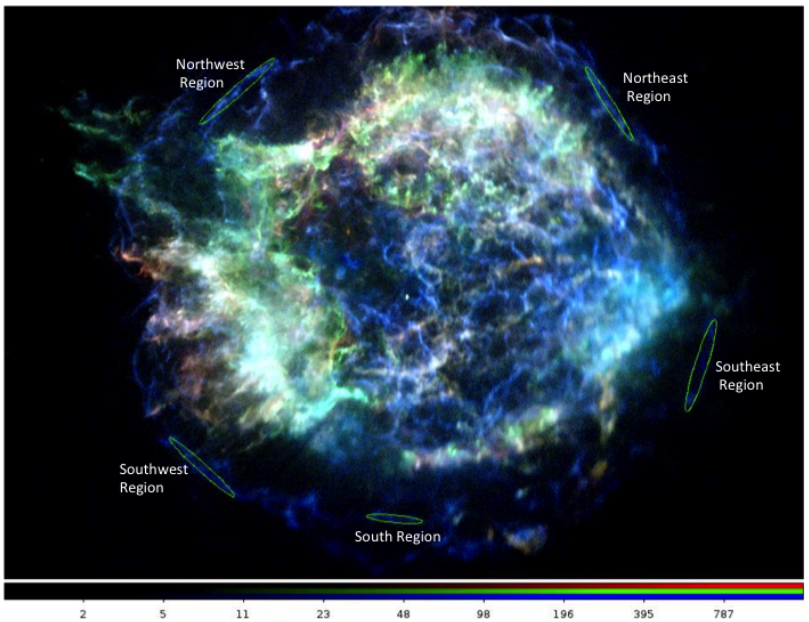

Figure 5.10. Cas A combined image with selected regions. Elliptical areas show the regions that spectral analysis were performed on.

- Response files, or the redistribution matrix files (RMFs), have been created for selected regions. RMF is mapping between the physical properties of incoming photons (such as their energy) and their detected properties (such as detector pulse heights or PHA) for a given detector. This mapping is stored in the form of a 2-D matrix. *mkacisrmf* tool of the CIAO 4.4 was used to create the files.
- Ancillary Response Files (ARFs) have been generated by *mkarf* tool of CIAO 4.4. The ARF gives the effective area vs. energy for a given observation and instrument configuration; it has units of cm^2counts/photon. In order to create the arf file, an asphist file used for all regions is needed. This asphist file bins the aspect solution into a 3D histogram of duration vs pointing offset and roll offset.

The spectrums of the regions have been extracted using *xspec* tool of HEASOFT and are fitted with non-thermal *xspec* model Power-law. The best fit spectral values are presented below. Reduced chi-squared values between 1.36 - 1.51 are found for regions chosen. We added some Gaussian components to model the lines at around 1.0 keV, 1.3 keV, 1.85 keV, 2.40 keV and 6.55 keV, which we attribute

to Fe xxı, Mg xı, Si K xıı, S K xv and Fe Kα line emissions respectively.

(ii) *Modeling the Spectrums*: *Xspec* tool of HEASOFT package was used to model the spectrums. Regions were modeled by *wa(pow)* model to fit the spectrums associated with non-thermal emissions. Model explanations are given in the following:

- *Powerlaw*:

  Powerlaw model is a simple photon power law. It explains the relationships between two quantities. When the flux of photon distribution varies as a power of energy of the photons, this distribution follows a power law.

  A(E)=k.E^{α}

  Where α = photon index of power law (dimensionless) and K = norm ($keV^{-1}cm^{-1}s^{-1}$ at 1 keV)

- *Wabs*:

  This additive model is a photo-electric absorption using Wisconsin cross-sections.

$$M(E) = \exp(n_H \sigma_E(E))$$

  Where σ_E(E) is the the photo-electric cross-section and n_H is the equivalent hydrogen column density (in units of 10^{22} atoms cm^{-2})

- *Gaussian*:

  This is a simple gaussian line profile. If the width is ≤ 0 then it is treated as a delta function. Gaussians in the model fitting is used for the line emission of the elements.

$$A(E) = K_T \exp(\frac{(E - E_l)^2}{2\sigma^2})\sigma(2\pi)^{\frac{1}{2}}$$

  Where E_l is the line energy in the units of keV, σ_w is the line width in the units of keV, and K_T is the total photons in units $cm^{-2}s^{-1}$ in each element line.

Chandra x-ray spectra of northwest, northeast, southeast, south, southwest, and west regions are fitted with non-thermal power-law model which are shown in Figures from 5.11 to 5.15, respectively. The best fit model parameters for these regions are listed in Tables from 5.2 to 5.6 respectively. χ^2/dof is the reduced chi-squared of the fit. Additionally, 4 areas were arbitrarily selected from closer regions to the center. The selected region can be seen in Figure 5.16. The spectra of these regions were fitted by non-thermal power-law. Much more line emission are applied to the model, but as expected we could not find reasonable spectral values from these fittings, because the values of χ^2/dof were found as 7.76, 9.85, 13.72, and 8.56 for the regions inside 1, 2, 3, 4, respectively. For inside 1 and inside 2 regions, spectral distributions were given in Figure 5.17, top and bottom, respectively. Like wise, energy spectrums of inside regions 3 and 4 can be seen at the top and bottom panel of Figure 5.18 respectively. These high reduced chi-squared values are expected, because in the inside regions of Cas A thermal radiation is dominating over the non-thermal radiation.

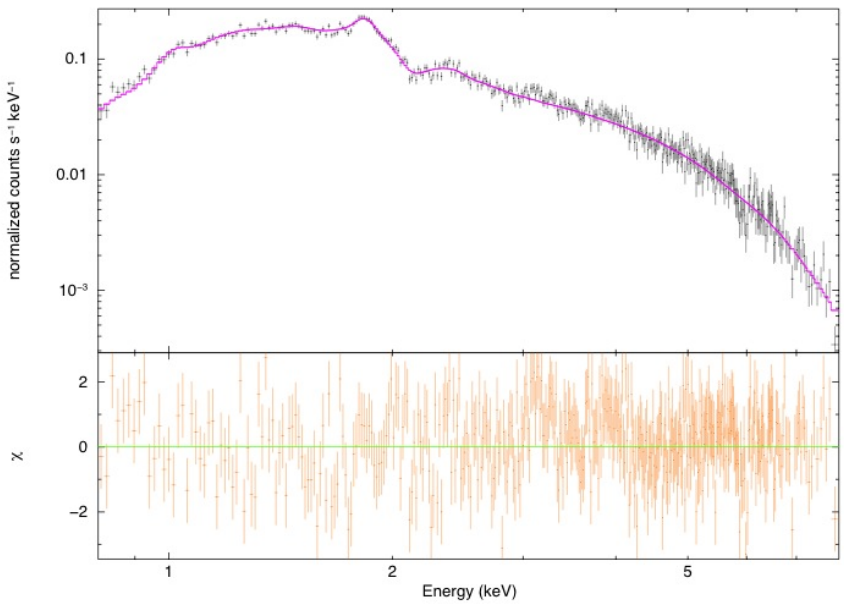

Figure 5.11. X-ray spectrum of the northwest region of Cas A.

Table 5.2. Best fit spectral values of the northwest region of Cas A.

	Value	**Unit**
Power Law Photon Index	2.25 ± 0.02	
Wabs	1.05 ± 0.02	10^{22} atoms cm^{-2}
Power Law Norm	$(1.67 \pm 0.05) \times 10^{-3}$	photons keV^{-1}cm^{2} s
χ^2/dof	1.36	
Line Emission - Fe xxı	1.06 ± 0.011	keV
Line Emission - Si K xıı	1.88 ± 0.005	keV
Line Emission S K xv	2.43 ± 0.002	keV

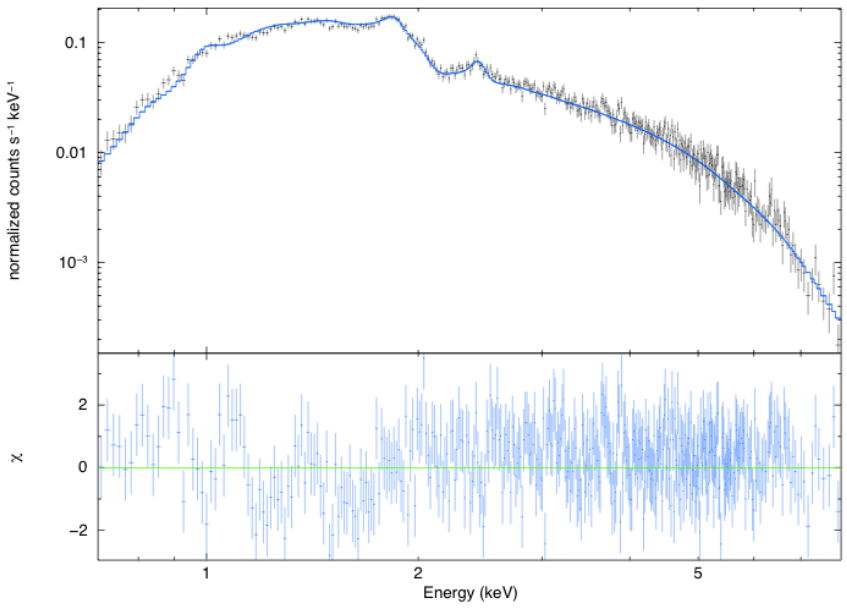

Figure 5.12. X-ray spectrum of the northeast region of Cas A.

Table 5.3. Best fit spectral values of the northeast region of Cas A.

	Value	**Unit**
Power Law Photon Index	2.66 ± 0.02	
Wabs	1.25 ± 0.01	10^{22} atoms cm^{-2}
Power Law Norm	(2.15 ± 0.06)×10^{-3}	photons keV^{-1}cm^2 s
χ^2/dof	1.41	
Line Emission - Fe xxi	1.01 ± 0.007	keV
Line Emission - Si K xiii	1.87 ± 0.007	keV
Line Emission - S K xv	2.44 ± 0.009	keV

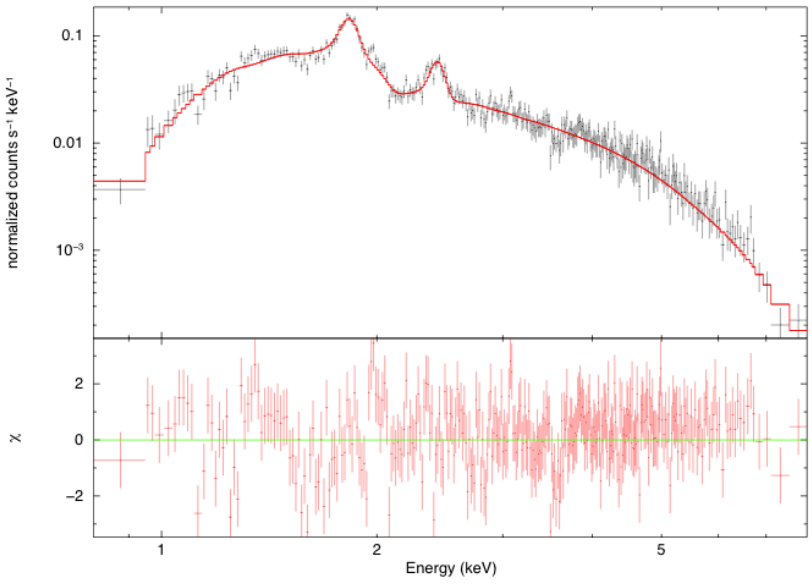

Figure 5.13. X-ray spectrum of the southeast region of Cas A.

Table 5.4. Best fit spectral values of the southeast region of Cas A.

	Value	**Unit**
Power Law Photon Index	3.21 ± 0.04	
Wabs	2.08 ± 0.08	10^{22} atoms cm^{-2}
Power Law Norm	(1.15 ± 0.07)×10^{-2}	photons keV^{-1}cm^2 s
χ^2/dof	1.52	
Line Emission - Fe xxı	1.05 ± 0.005	keV
Line Emission - Mg xı	1.38 ± 0.006	keV
Line Emission - Si K xıı	1.87 ± 0.002	keV
Line Emission - S K xv	2.44 ± 0.005	keV
Line Emission - Fe Kα	6.49 ± 0.004	keV

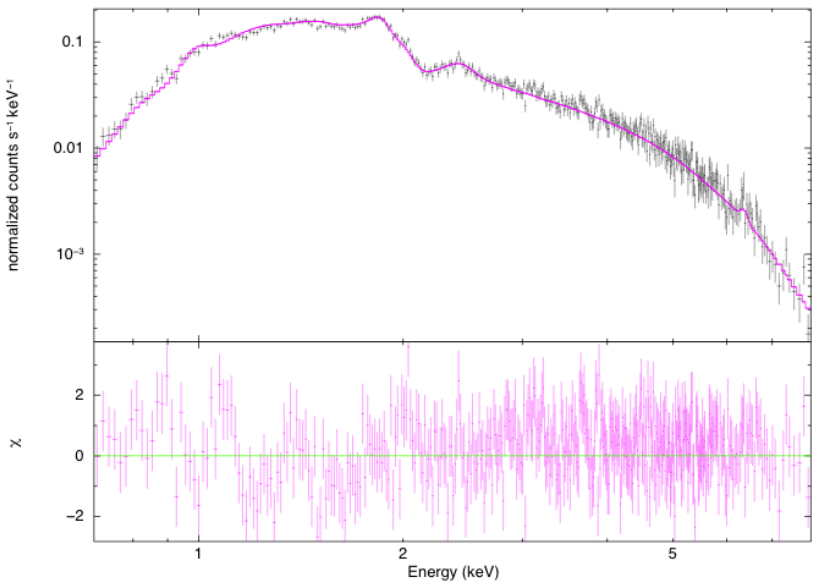

Figure 5.14. X-ray spectrum of the south region of Cas A.

Table 5.5. Best fit spectral values of the south region of Cas A.

	Value	**Unit**
Power Law Photon Index	2.65 ± 0.02	
Wabs	1.24 ± 0.02	10^{22} atoms cm^{-2}
Power Law Norm	(2.11 ± 0.06)×10^{-3}	photons keV^{-1}cm^2 s
χ^2/dof	1.47	
Line Emission - Fe xxı	1.02 ± 0.007	keV
Line Emission - Si K xıı	1.87 ± 0.006	keV
Line Emission - S K xv	2.46 ± 0.001	keV
Line Emission - Fe Kα	6.41 ± 0.008	keV

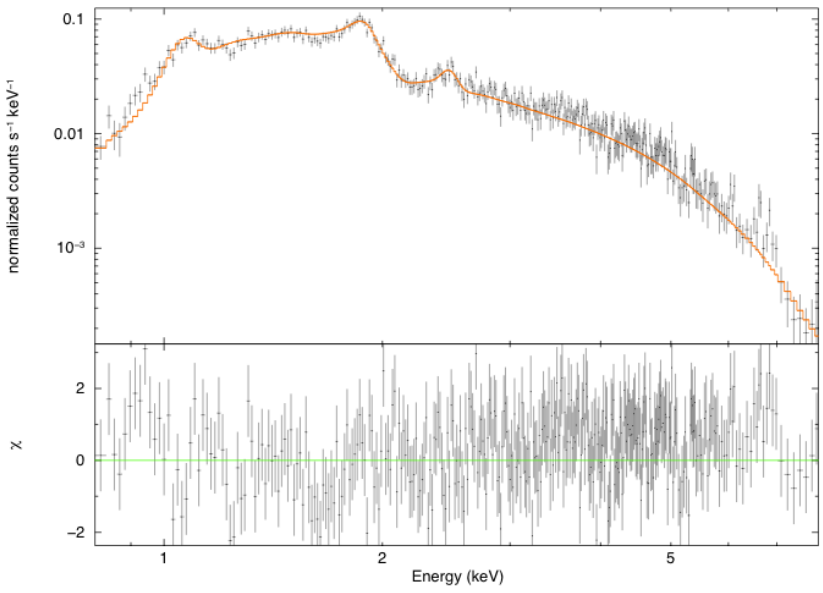

Figure 5.15. X-ray spectrum of the southwest region of Cas A.

Table 5.6. Best fit spectral values of the southwest region of Cas A.

	Value	**Unit**
Power Law Photon Index	2.62 ± 0.04	
Wabs	1.44 ± 0.04	10^{22} atoms cm^{-2}
Power Law Norm	(1.13 ± 0.06)×10^{-2}	photons keV^{-1}cm^2 s
χ^2/dof	1.44	
Line Emission - Fe xxı	1.04 ± 0.005	keV
Line Emission - Si K xıı	1.88 ± 0.007	keV
Line Emission- S K xv	2.47 ± 0.036	keV

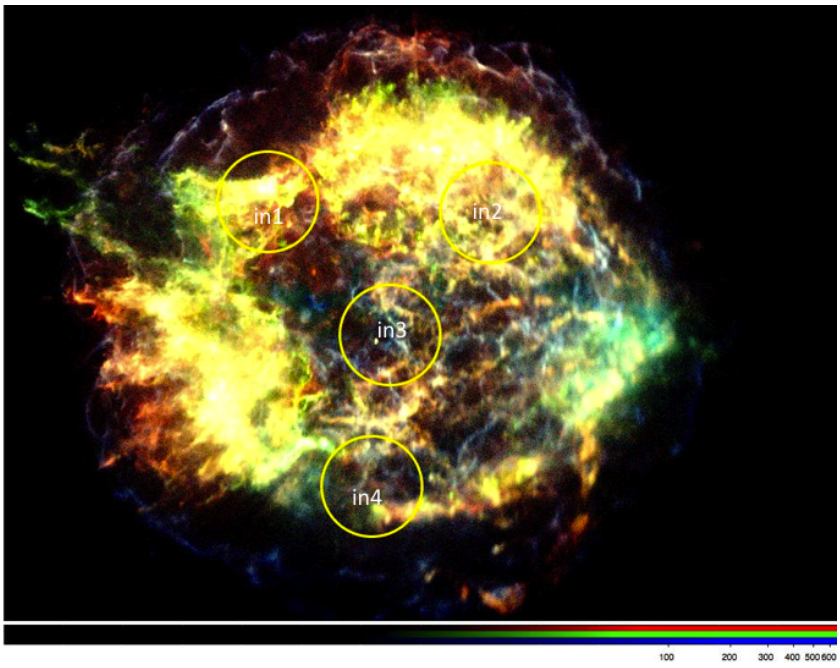

Figure 5.16. X-ray image of Cas A with regions selected inside.

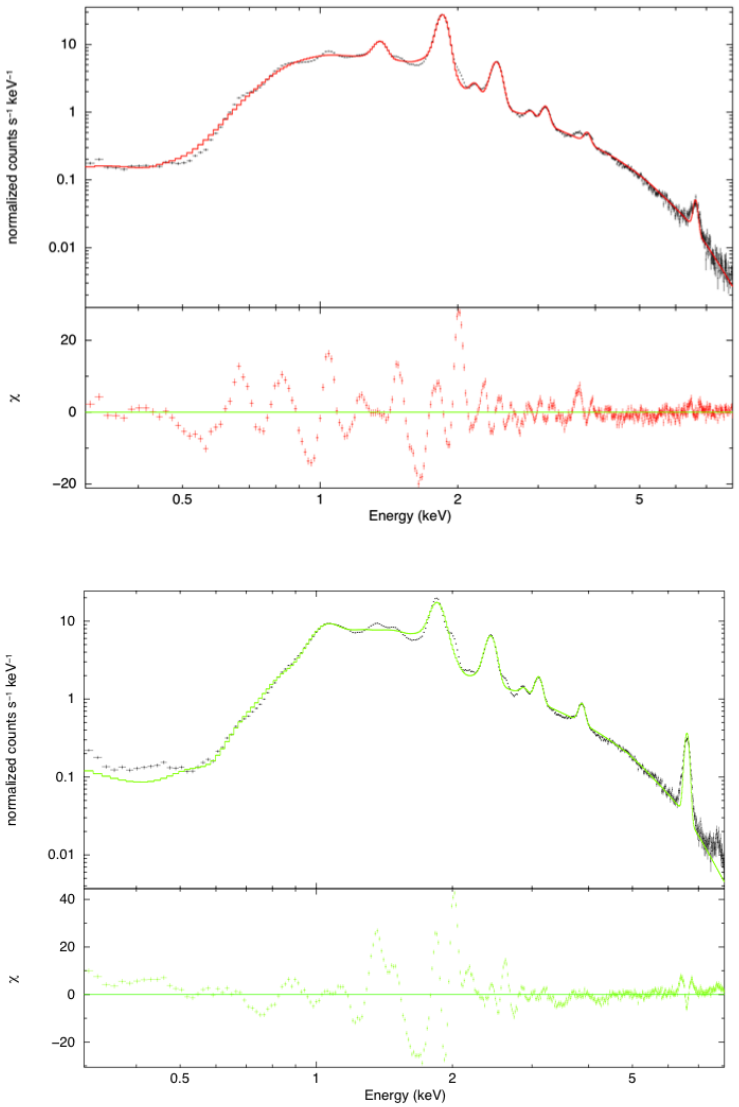

Figure 5.17. Chandra X-ray spectrum of inside region 1 and 2 of Cas A, top and bottom panels, respectively.

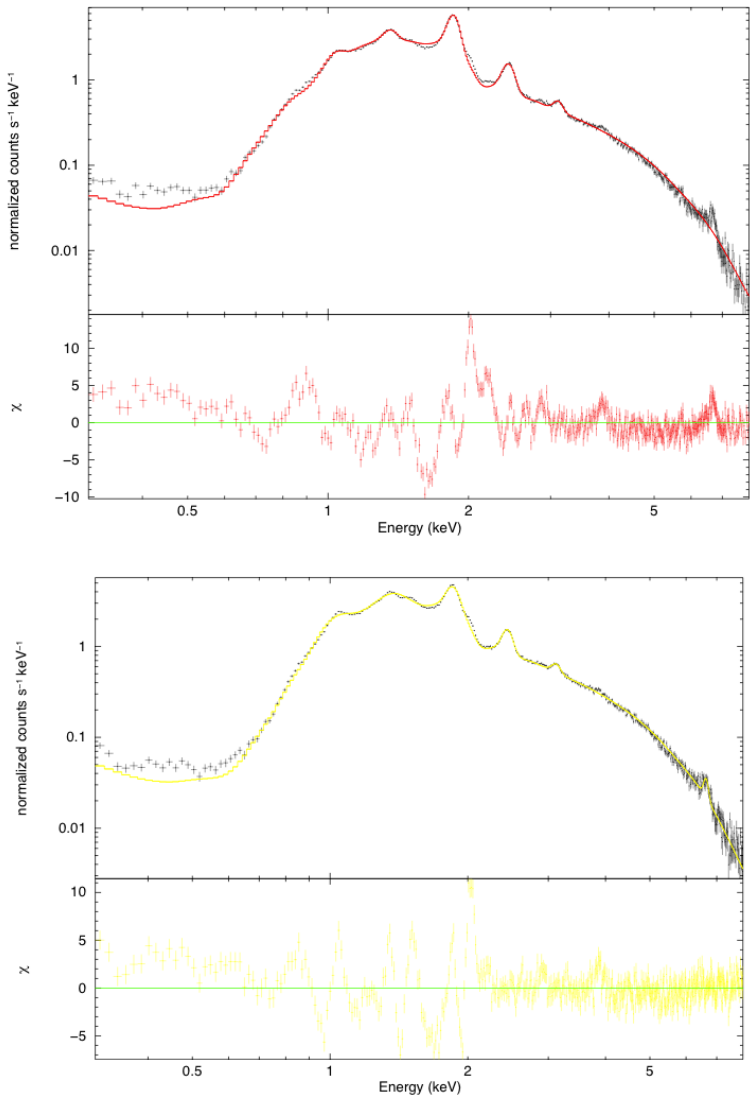

Figure 5.18. Chandra X-ray spectrum of inside region 3 and 4 of Cas A, top and bottom panels, respectively.

5.2. TYCHO

5.2.1. Overview of the Previous Results of Tycho

Tycho's SNR, also called SN 1572 or SNR120.1+01.4 is classified as a Type Ia SN explosion [35] . Tycho is the spherical SNR of the supernova exploded in 1572 with a diameter of $\sim$ 8' [35]. Expansion of Tycho has been observed in the radio by VLA telescope [37]. It's average radio expansion parameter is found to be 0.47. The radio flux is 40.4 Jy at 1.4 GHz with a spectral index of 0.65 [38]. The radio emission is also consistent with the acceleration of cosmic ray electrons by the forward shock [39]. Infrared observations of AKARI between 9 and 160 μ reveal thermal dust emission in the northeast and northwest shells. The expansion is also observed by Chandra [40] with the expansion rate of 0.52. While X-ray spectrum [41] is dominated by very strong line emissions of Si, S and Fe, the major fraction (%60) of the X-ray continuum emission comes from non-thermal synchrotron [42]. This is an expected result for such a young SNR. The shocked ejecta velocity is calculated to be about 4700 km/s for Si, S and Ar [43]. The claimed distance is 3 to 5 kpc on considering of the measured proper motion. However H I absorption studies [45] calculated the distance between 2.5 and 3 kpc. The Fermi LAT Collaboration announced a detection in the energy range from $\sim$0.4 to 100 GeV. The integrated spectrum is found as $3.5 \pm (1.1_{stat}) \pm (0.7_{syst}) \times 10^{-9} \mathrm{cm}^{-2}\mathrm{s}^{-1}$ with a photon index of $2.3 \pm (0.2_{stat}) \pm (0.1_{syst})$ [46]. Detection of non-thermal X-ray synchrotron emission from the rims of the remnant of Tycho suggests that the shocks in SNRs can accelerate cosmic ray particles up to TeV energies [48]. This idea is supported by VERITAS observations, they declared a TeV detection with a flux of %0.9 of Crab Nebula [47].

5.2.2. Fermi-LAT Analysis of Tycho

Fermi observation of Tycho between the dates 08.04.2008 and 05.17.2012 was used in the analysis. Total exposure time was nearly 43 months 8 PH and a SC files were handled as data set. Tycho Fermi data was extracted from the position right ascension (RA) : 6.40^o and declination (Dec) : 64.12^o. Likewise in the case of Cas A,

the LAT data in the region of 20^o and in the energy range of 200 MeV - 300 GeV was required from Fermi Science Support Center (FSSC's) web site data server.

5.2.2.1. Data Preparation. The same analysis processes were applied to the Tycho's Fermi data set like in the case of Cas A. *gtselect* and *gtmktime* tools were used in data reduction. Zenith angle was selected to be 105^o and, the analysis was performed in the energy range between 200 MeV and 200 GeV. Also, rock angle of 52^o was used to eliminate pointed observations from the data.

5.2.2.2. Creating Count Cube and Map. The count cube and the count map of the region of interest was created by CCUBE and CPMAP options of *gtbin* tool respectively. For Tycho analysis, size of the X and Y axis in pixels was selected to be both 80, image scale was 0.1^o/pixel and 5 number of logarithmically uniform energy bins were used. The analysis region is shown in Figure 5.19.

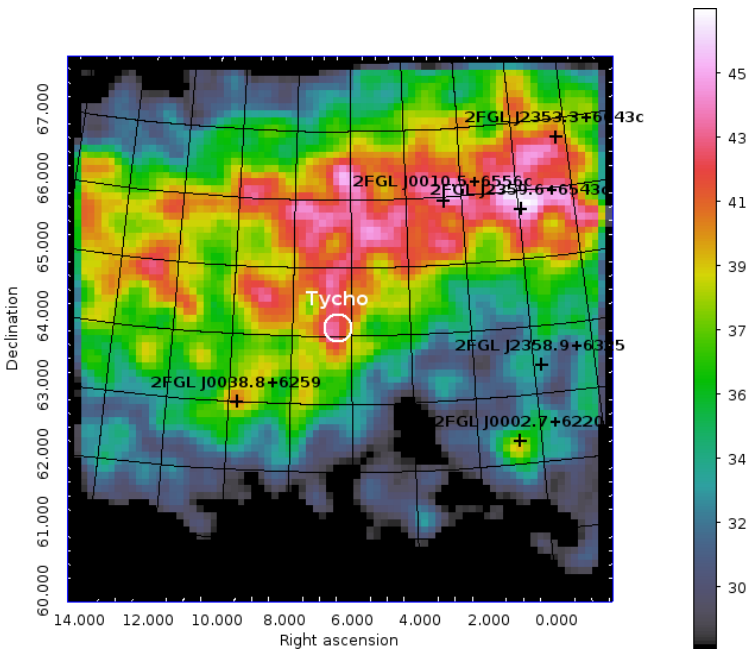

Figure 5.19. Fermi $8^o \times 8^o$ counts map of Tycho smoothed with 3σ in the energy range of 0.2 - 200 GeV.

5.2.2.3. Building Background Model. The XML file including all the background sources was created with respect to distances and the significances of the point sources in the analysis region using Fermi 2nd year catalog. The sources having the distance smaller than $\sim 6^o$ and having significance bigger than 5σ were selected. Background model consists of 9 point sources chosen within the analysis region. Also galactic diffuse component (*gal_2yearp7v6_v0*) and isotropic extragalactic emission (*iso_p7v6source*) were added to the model. Table 5.7 shows the distances and the significances of background sources. In the XML file, we fixed all parameters of sources that lay outside the region with the radius of 4^o. We only kept fixed all parameters of 2FGLJ0038.8+6259 which lies within the 4^o radius.

Table 5.7. Background point sources located within the radius of 6^o around the location of Tycho.

	Distance to ROI Center (degree)	**Significance (σ)**
2FGLJ0002.7+6220	3.14	13.67
2FGLJ0007.7+6825c	4.66	6.19
2FGLJ0010.5+6556c	2.42	7.72
2FGLJ0035.8+5951	4.42	15.06
2FGLJ0038.8+6259	1.83	5.60
2FGLJ2353.3+6643c	4.25	5.37
2FGLJ2359.4+6751c	4.59	7.73
2FGLJ2359.6+6543c	3.20	7.71
2FGLJ0109.9+6132	5.62	32.89

5.2.2.4. Computing Maps and Binned Likelihood Analysis. *gtltcube* tool was used to calculate how much time the LAT has observed Tycho at the position RA : 6.40^o and Dec : 64.12^o. Exposure map of Tycho was produced by *gtexpcube2* tool with sizes for the X and Y axes to be 400 pixels each and image scale was 0.1 degree/pixel, and 5 bins were used in the energy range of 200 MeV to 200 GeV. The exposure map was

performed using the IRF P7SOURCE_V6. The source map was similarly computed by *gtsrcmaps* tool. Exposure map and count cube were used to create the source map. Similar to Cas A gamma-ray analysis, binned likelihood method was applied to Tycho.

5.2.2.5. Fermi Analysis Results of Tycho. Fermi analysis clearly showed the source at a significance level 8σ (TS value of 64.4) with integral photon flux of $(1.88 \pm 0.2)\times10^{-8}$ photons cm^{-2}s^{-1}. Spectral index was found to be $\Gamma = 2.97 \pm 0.2_{stat}$. Tycho is a fainter object in comparison to Cas A in gamma-ray. In order to demonstrate the detection of Tycho, a residual map was constructed. First a $8^o\times8^o$ count map was produced for Tycho. *gtmodel* tool was used with the XML model file including Tycho and to create an output model counts map. We subtracted this model counts map from the original counts map to obtain residual map. The same step was repeated by removing Tycho from our background xml file. So we had two residual maps one showing Tycho and the other not. The the existence of Tycho in the region of interest can be clearly seen on the right panel of Figure 5.20.

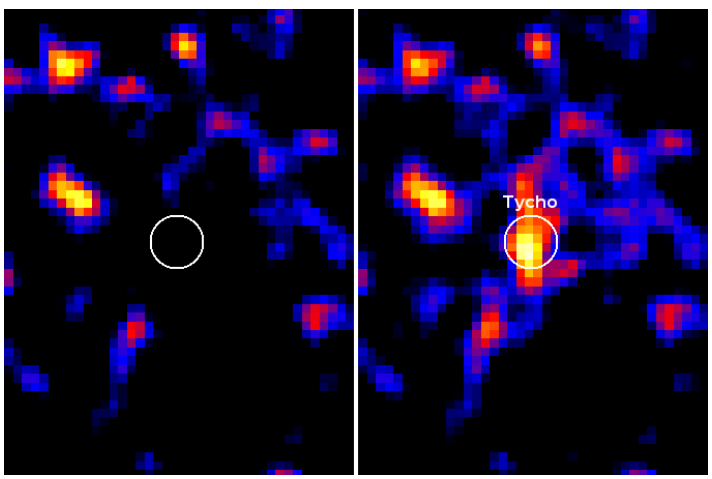

Figure 5.20. Residual map of Tycho smoothed with 3σ. The left map was built with background XML model file including Tycho. The right map was built with background XML file not including Tycho. The difference shows the detection of Tycho. The residuals are ranging between -6.5 and +6.5 counts and Tycho is visible in the range of +0.9 - +5.8 counts.

5.2.3. Chandra Analysis of Tycho

Chandra-1-ms observation of Tycho is performed on 4 combined S3 CCD chips (I0, I1,I2, and I3) of ACIS. Observation ID is 10095 (Hughes), the exposure time for the point RA: 00h 25' 19" DEC: 64^o 08' 10" is 175670 s and the observation date is April 2009. The observation is in timed readmode and faint datamode.

5.2.3.1. Data Reduction. The same data reduction method used in Chandra analysis of Cas A was used in the analysis of Tycho. The following steps were applied to *event1* data file:

- Reproducing Chandra tata
- Removing *destreak* events
- Checking observation mode and clearing the status
- Creating a new bad pixel file
- Generating a new level-1 file
- Filtering on grade, status and good time
- Applying energy cut

5.2.3.2. Image Analysis of Tycho. Similarly, *dmcopy* tool of *ciao4.4* was used to create the images and *ds9* software tool is used to display the images. The image for 0.3-8 keV energies was created to have a general look at SNR Tycho. Also three different energy bands of Tycho; 0.3-1.5, 1.5-2.5, and 2.5-8 keV images were created for soft, medium, and hard energies, respectively. The images (Figures 21-24) show clearly shell-like structure of Tycho. Also, a combined image of all energy bands is shown in Figure 5.25 together with ellipses drawn on the filaments to indicate analysis regions for spectral analysis (Section 5.2.3.3).

5.2.3.3. Spectral Analysis of Tycho. The spectral analysis applied to SNR Tycho is similar to the one appiled for Cas A. Chandra observation of Tycho has done on the 4 chips so that the *arf* files were created by using different *asphist* files with their

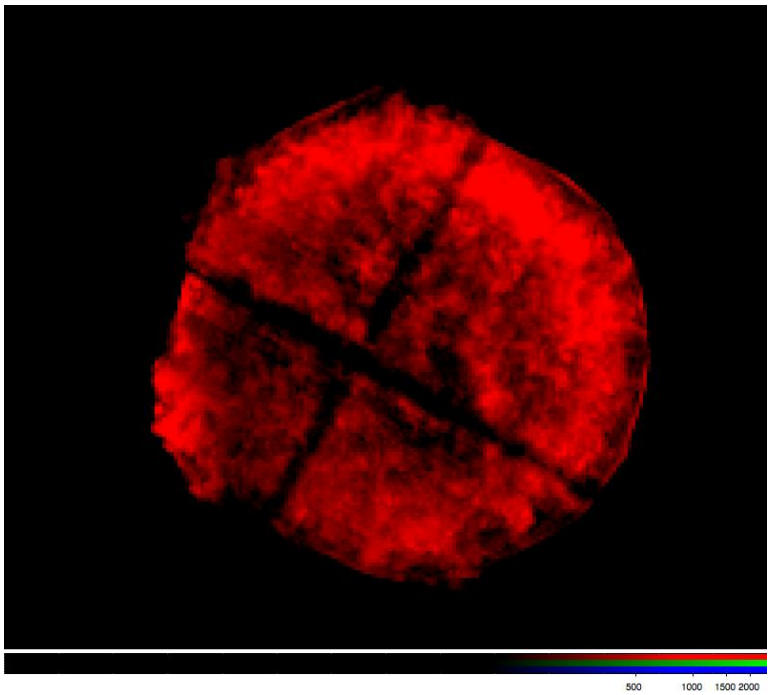

Figure 5.21. Tycho Chandra soft energy image in the range of 0.3 - 1.5 keV.

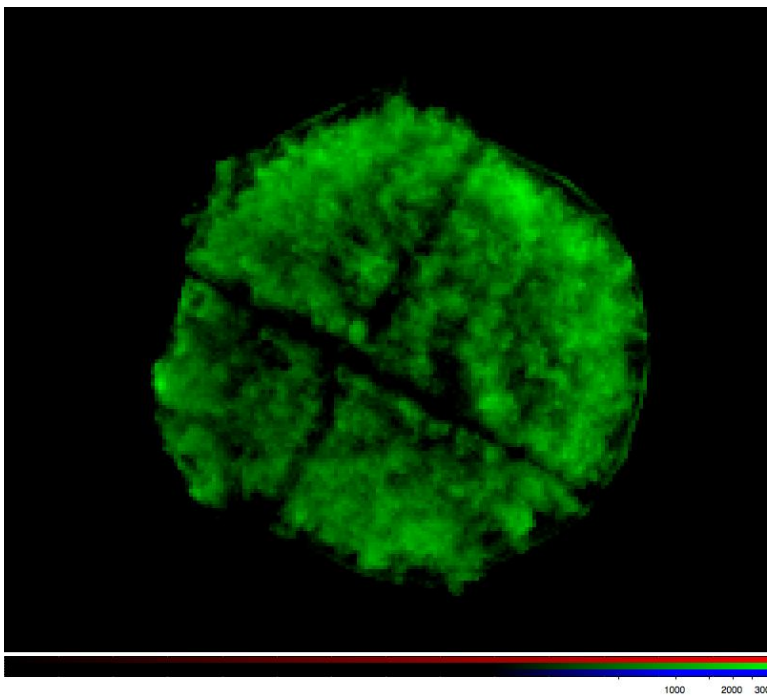

Figure 5.22. Tycho Chandra medium energy image in the range of 1.5 - 2.5 keV.

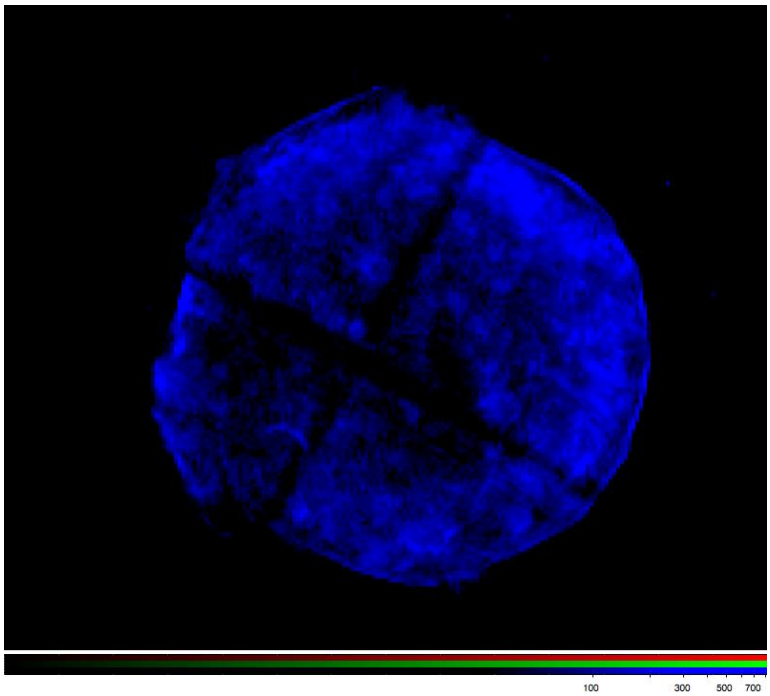

Figure 5.23. Cas A Chandra hard energy image in the range of 2.5 - 8 keV.

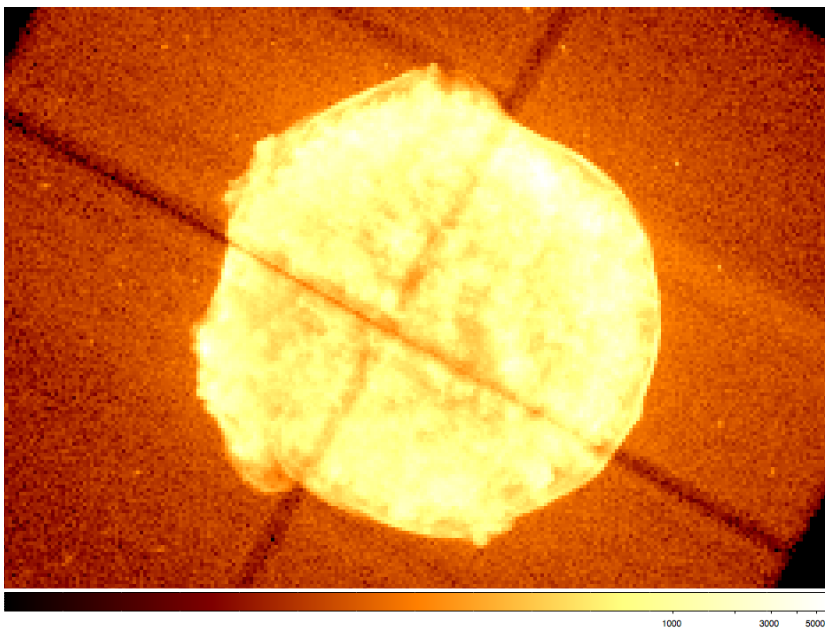

Figure 5.24. Tycho Chandra image in the range of 0.3 - 8 keV.

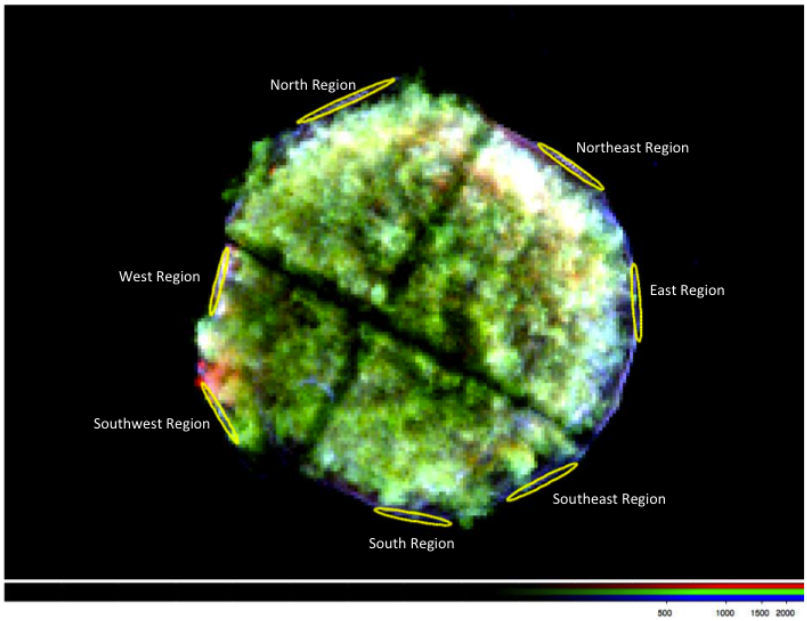

Figure 5.25. Tycho Chandra combined image of soft, medium, and hard energies with selected regions.

associated chips. 4 basic *pi* and response files were produced in the same way. 7 regions were selected from the thin shell of Tycho. The spectrums of the regions have been similarly extracted using *xspec* tool of HEASOFT and are fitted with power-law models. The best fit spectral values were presented in Tables from 5.8 to 5.14. Reduced chi-squared values between 1.18 and 1.46 were found. Gaussian components of the models were fit at around 1.0 keV, 1.3 keV, 1.85 keV, 2.40 keV and 6.55 keV, which we attribute to Fe xxı, Mg xı, Si K xıı, S K xv, and Fe Kα line emissions, respectively. These fits are shown in Figures from 5.26 to 5.32.

As in the Chandra analysis of Cas A, some internal regions of Tycho were analyzed. Figure 5.33 shows the selected regions. Same non-thermal power law models were fit the spectra. Figures 5.34 and 5.35 show spectral distribution of X-ray photons coming from inside Tycho modeled with power-law. However, reasonable chi-squared values could not be found. Thus, reduced chi-squared values of 14.12, 11.14, 13.43, and 9.75 were found for the regions 1, 2, 3, and 4, respectively.

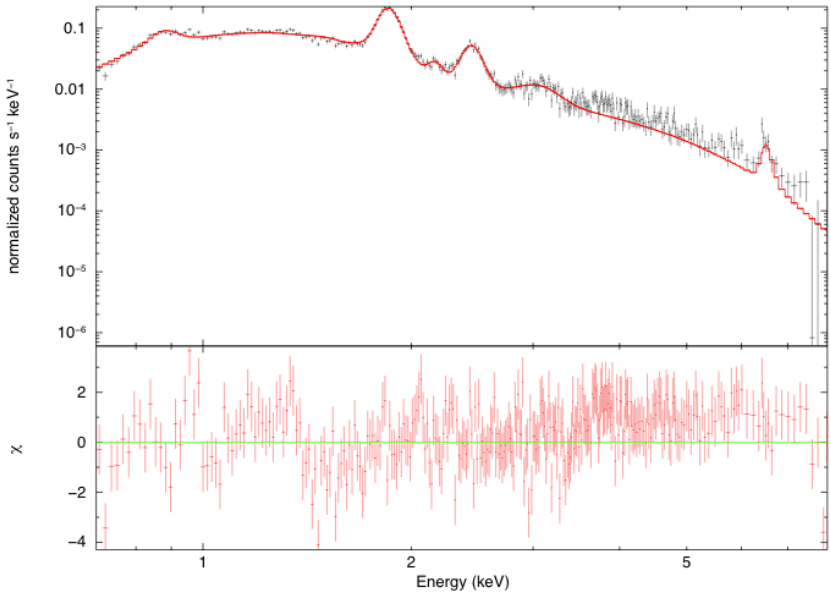

Figure 5.26. X-ray spectrum of the east region of Tycho.

Table 5.8. Best fit spectral values of the east region of Tycho.

	Value	**Unit**
Power Law Photon Index	2.78 ± 0.03	
Wabs	1.05 ± 0.02	10^{22} atoms cm^{-2}
Power Law Norm	(7.43 ± 0.031)×10^{-4}	photons keV^{-1}cm^{2} s
χ^2/dof	1.24	
Line Emission - Si K XIII	1.85 ± 0.003	keV
Line Emission - S K XV	2.44 ± 0.001	keV

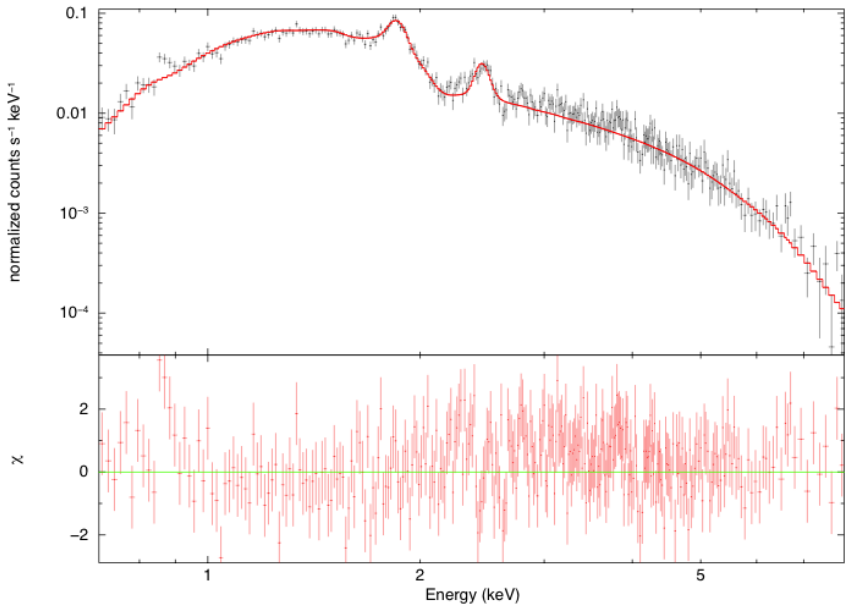

Figure 5.27. X-ray spectrum of the north region of Tycho.

Table 5.9. Best fit spectral values of the north region of Tycho.

	Value	**Unit**
Power Law Photon Index	3.31 ± 0.02	
Wabs	1.12 ± 0.03	10^{22} atoms cm^{-2}
Power Law Norm	(7.43 ± 0.32)×10^{-4}	photons keV^{-1}cm^{2} s
χ^2/dof	1.18	
Line Emission - Si K XIII	1.86 ± 0.002	keV
Line Emission - S K XV	2.44 ± 0.003	keV

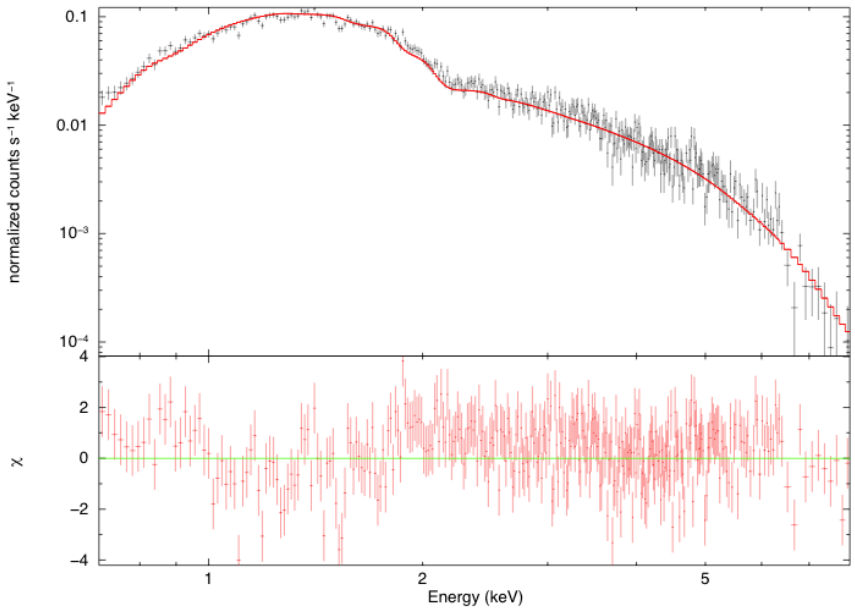

Figure 5.28. X-ray spectrum of the northeast region of Tycho.

Table 5.10. Best fit spectral values of the northeast region of Tycho.

	Value	**Unit**
Power Law Photon Index	2.95 ± 0.03	
Wabs	1.08 ± 0.02	10^{22} atoms cm^{-2}
Power Law Norm	(1.36 ± 0.41)×10^{-4}	photons keV^{-1}cm^2 s
χ^2/dof	1.44	

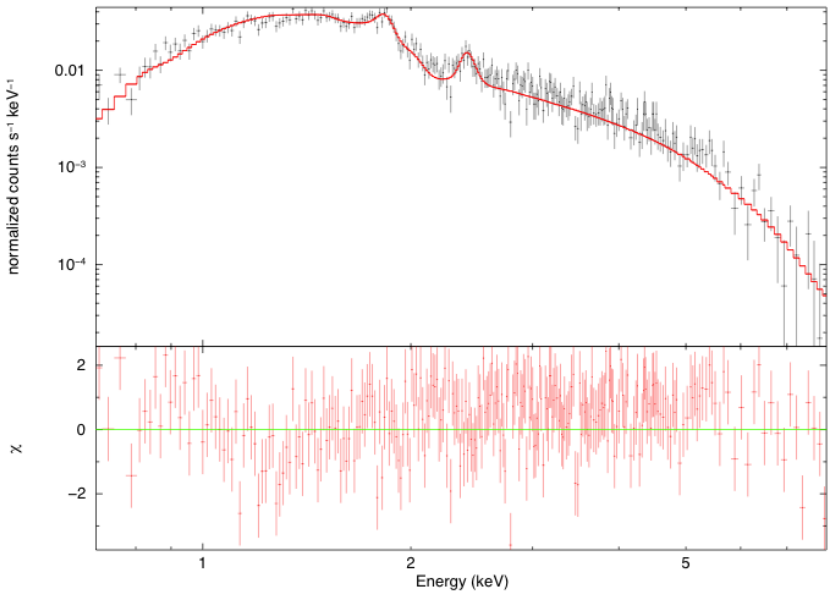

Figure 5.29. X-ray spectrum of the south region of Tycho.

Table 5.11. Best fit spectral values of the south region of Tycho.

	Value	**Unit**
Power Law Photon Index	2.98 ± 0.05	
Wabs	0.93 ± 0.03	10^{22} atoms cm^{-2}
Power Law Norm	(4.67 ± 0.2)×10^{-4}	photons keV^{-1}cm^2 s
χ^2/dof	1.22	
Line Emission - Si K XIII	1.84 ± 0.001	keV
Line Emission - S K XV	2.41 ± 0.002	keV

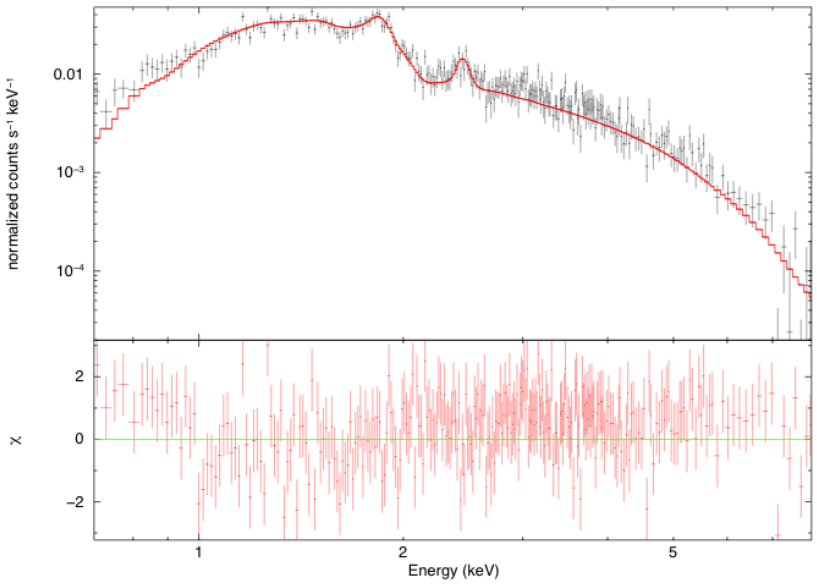

Figure 5.30. X-ray spectrum of the southeast region of Tycho.

Table 5.12. Best fit spectral values of the southeast region of Tycho.

	Value	**Unit**
Power Law Photon Index	2.89 ± 0.05	
Wabs	1.02 ± 0.03	10^{22} atoms cm^{-2}
Power Law Norm	(4.59 ± 0.3)×10^{-4}	photons keV^{-1}cm^2 s
χ^2/dof	1.19	
Line Emission - Si K XIII	1.85 ± 0.005	keV
Line Emission - S K XV	2.44 ± 0.001	keV

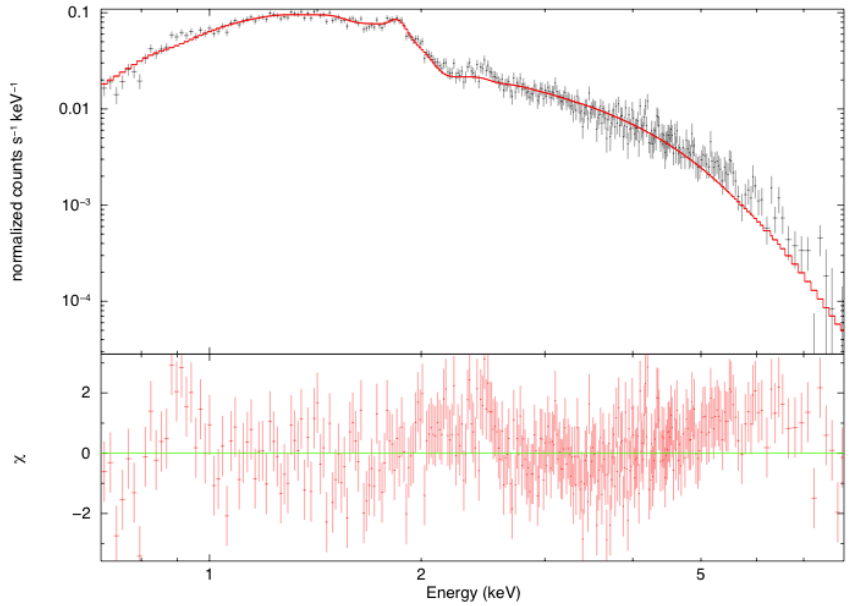

Figure 5.31. X-ray spectrum of the southwest region of Tycho.

Table 5.13. Best fit spectral values of the southwest region of Tycho.

	Value	**Unit**
Power Law Photon Index	2.89 ± 0.05	
Wabs	1.02 ± 0.03	10^{22} atoms cm^{-2}
Power Law Norm	(4.59 ± 0.3)×10^{-4}	photons keV^{-1}cm^2 s
χ^2/dof	1.19	
Line Emission - Fe xxı	1.02 ± 0.003	keV
Line Emission - Si K xıı	1.86 ± 0.008	keV
Line Emission - S K xv	2.45 ± 0.003	keV

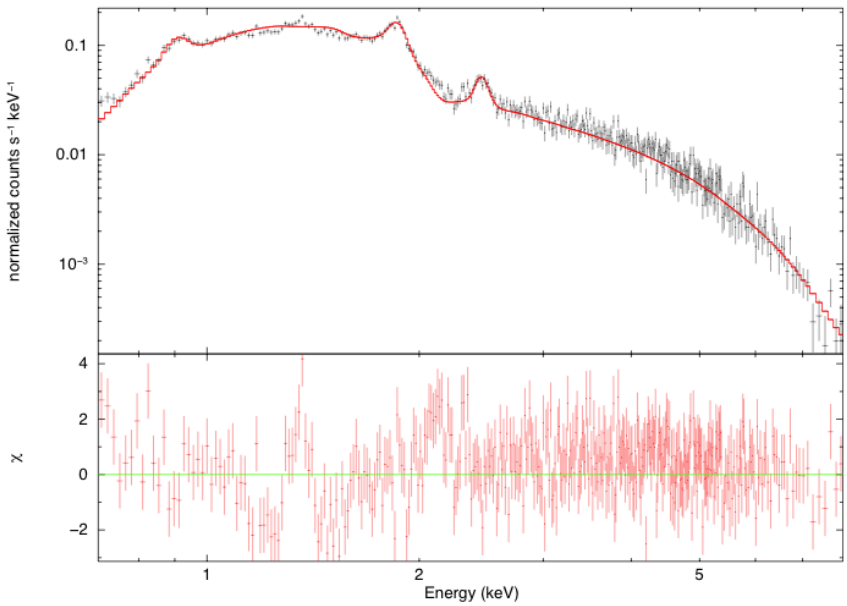

Figure 5.32. X-ray spectrum of the west region of Tycho.

Table 5.14. Best fit spectral values of the west region of Tycho.

	Value	**Unit**
Power Law Photon Index	3.19 ± 0.04	
Wabs	0.92 ± 0.02	10^{22} atoms cm^{-2}
Power Law Norm	(7.91 ± 0.3)×10^{-4}	photons keV^{-1}cm^2 s
χ^2/dof	1.46	
Line Emission - Fe xxı	0.97 ± 0.004	keV
Line Emission - Si K xıı	1.85 ± 0.001	keV
Line Emission - S K xv	2.44 ± 0.005	keV
Line Emission - Ar xvıı	3.05 ± 0.002	keV
Line Emission - Fe Kα	6.51 ± 0.005	keV

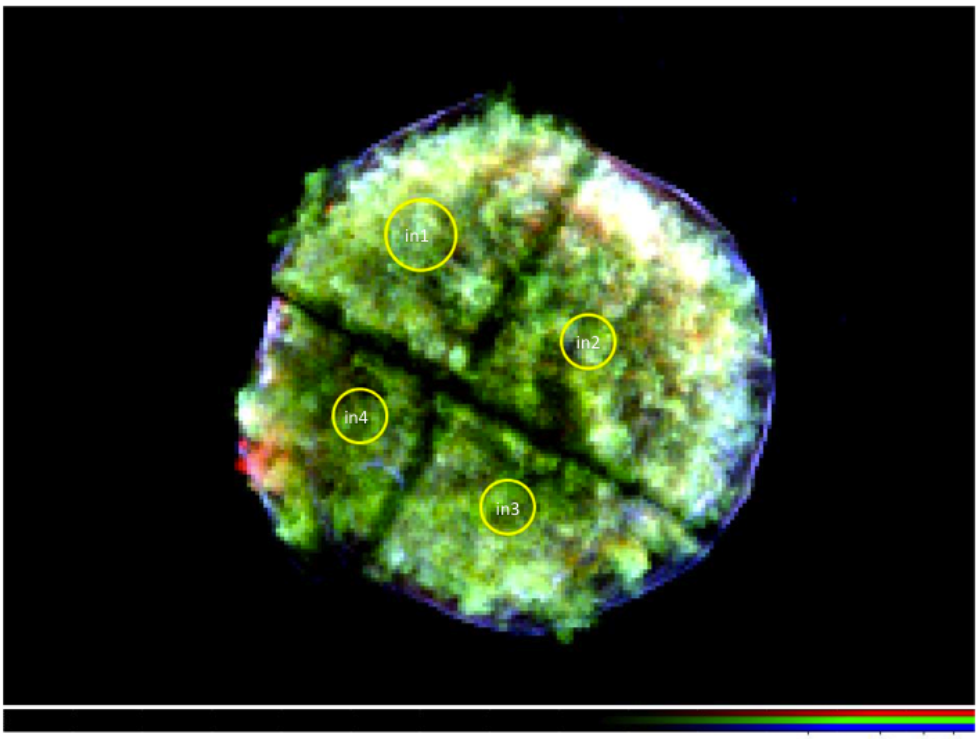

Figure 5.33. The Chandra combined image of soft, medium, and hard energies with selected regions from Tycho.

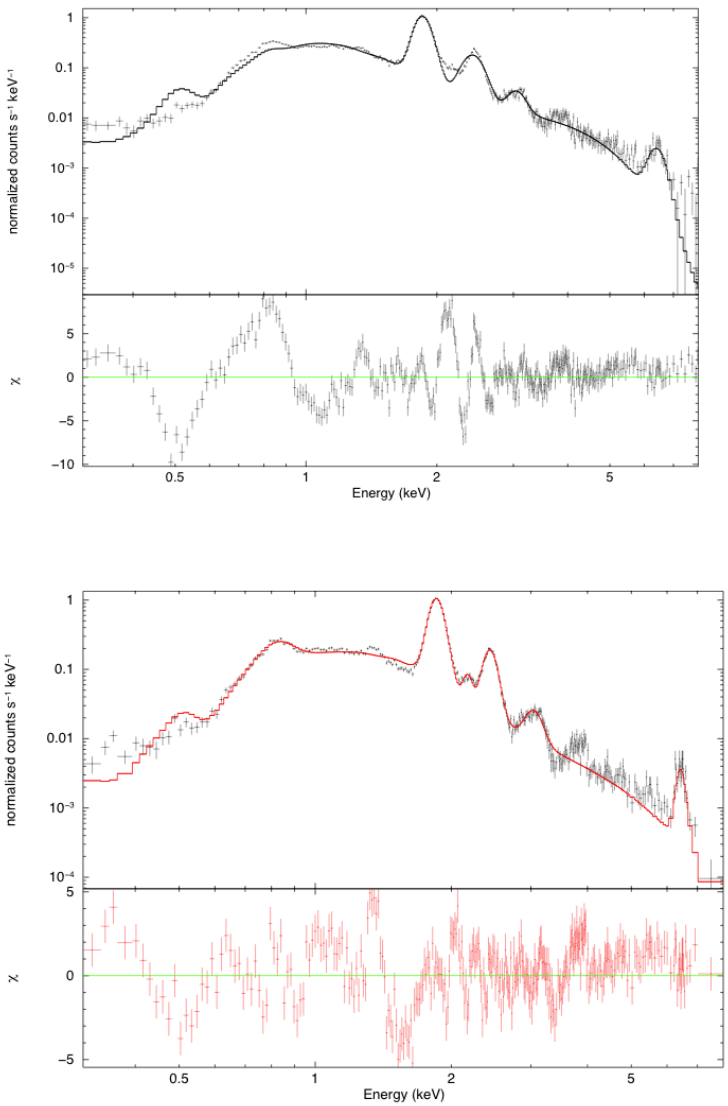

Figure 5.34. Chandra X-ray spectrum of inside regions 1 and 2 of Tycho, top and bottom panels, respectively.

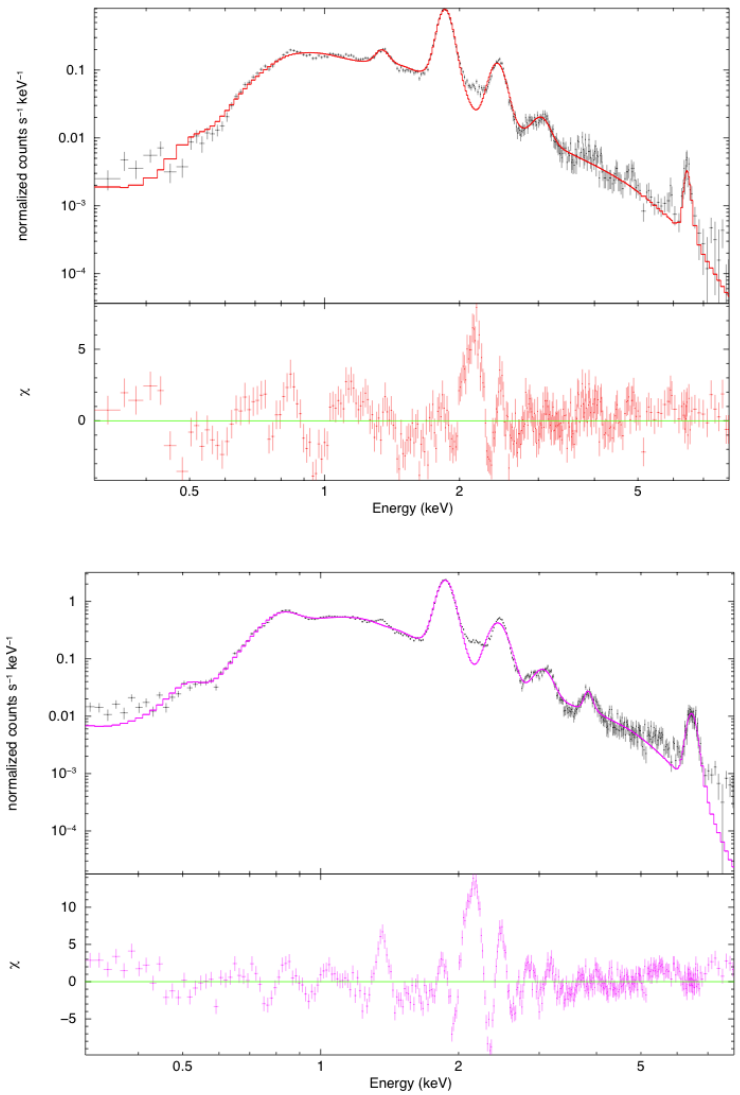

Figure 5.35. Chandra X-ray spectrum of inside regions 3 and 4 of Tycho, top and bottom panels, respectively.

6. SUMMARY AND DISCUSSION

In this thesis, young SNRs Cas A and Tycho were studied in the energy ranges of 0.5 - 50 GeV and 0.2 - 200 GeV, respectively by Fermi-LAT to find out if these remnants are gamma-ray emitters. The aim is to answer the question of which regions of young, shell-type SNRs are dominant emitters for non-thermal radiation. Therefore Chandra-ACIS analysis of Cas A and Tycho were also performed at 0.3 - 8 keV.

SNRs have the mechanism that can accelerate the particles up to TeV energies. In order to explain at least obliquely the existence of these high energy charged particles, we need to detect GeV photons produced by neutral pion decay, inverse Compton, and relativistic bremsstrahlung processes in SNRs. We observed Cas A in gamma-ray at the significance of 26σ with a integral photon flux of $(17.6 \pm 0.11) \times 10^{-9}$ photons $cm^{-2}s^{-1}$ for the given energy range. Also, the photon index of Cas A was found to be 2.02 ± 0.04. We could clearly locate Cas A on the created $8^o \times 8^o$ counts map and we could produce spectral distributions of significance, counts, and flux with respect to energy. The results can be seen in the Section 5.1.2.6. Fermi-LAT collaboration has declared significance level of 12.2σ and the integral photon flux above 500 MeV of $(8.7 \pm 1.3) \times 10^{-9}$ photons $cm^{-2}s^{-1}$ for Cas A at this energy range [57]. In Fermi-LAT analysis of Tycho, the integral photon flux of $(18.9 \pm 2.8) \times 10^{-9}$ photons $cm^{-2}s^{-1}$ and photon index of 2.98 ± 0.20 were measured with a significance of 8σ. Fermi-LAT collaboration has announced gamma-ray analysis results of Tycho significance of 5σ and, the integral photon flux of $(3.5 \pm 1.1_{stat} \pm 0.1_{syst}) \times 10^{-9}$ photons $cm^{-2}s^{-1}$ and photon index of $2.3 \pm 0.2_{stat} \pm 0.1_{syst}$ [46]. The differences in the values of flux and significance between our analysis and what Fermi-LAT has announced mainly arises from exposure times, because we used almost 1392 days of observations for Cas A but LAT collaboration detected Cas A in 394 days exposure. Also, for Fermi-LAT analysis of Tycho, we used 11 months more data than Fermi-LAT collaboration has used. In the Fermi-LAT analysis of Tycho we found relatively low flux and significance values in comparison to Cas A. Since Tycho is a weak source, a residual map was built to show SNR Tycho in $8^o \times 8^o$ region by removing Tycho from background XML file. We

got detection of Cas A and Tycho with the highest level of significance so far. So, Fermi-LAT analyses of Cas A and Tycho show that young SNRs are one of the main GeV sources in the Galaxy and imply that they are essential candidates of cosmic ray acceleration.

The diffuse shock acceleration theory of Fermi has claimed that strong magnetic field originated from shock energy coming from SN explosion accelerates the particles up to very high energies. The X-rays are produced in high magnetic fields by process synchrotron emission which favors power-law energy distribution. In X-ray analysis of shell-like SNRs, these shock regions can be observed in thin filaments at the shell structures of remnants. So, we concentrated on the shells of the SNRs. The thin filaments selected from different parts of the shells of Cas A and Tycho were analyzed in the X-ray band. Extracted spectrums have been fitted with power-law model predicting the non-thermal emission component. Also, some gaussian components were added to the models to meet line emission peaks of elements for related energies. Reasonable chi-squared values, for example 1.36 - 1.51 for Cas A and 1.18 - 1.46 for Tycho have been found in the analyses. In the Chandra-ACIS analysis, we could show more thin filaments to be fitted with *xspec*'s power-law model and got lower chi-squared values for Tycho. However, spectrums of the regions chosen inside the SNRs could not be fitted with this non-thermal power-law model. For the inside analysis, we selected the regions in different locations and with different sizes randomly and we measured reduced chi-squared values close to each other. The reduced chi-squared values were obtained between 7.76 and 13.72 for the inside regions of Cas A, and between 9.75 and 14.12 for Tycho. Additionally, Cas A and Tycho evolutionarily are in the transition phases. So, it is not expected that the central regions have hard (2.5 - 8 keV) X-ray emissions [15]. As a result, Chandra analyses of Cas A and Tycho supported the idea of diffuse shock acceleration that accelerated particles reaching such high energies would be found in the forward shock regions.

REFERENCES

1. Hess, V. F., "Penetrating Radiation in Seven Free Ballon Flights", *Physics Zeits*, Vol. 13, No. 1084, 1912.

2. Koyama, K., R. Petre, E. V. Gotthelf, U. Hwang, M. Matsuura, M. Ozaki and S. S. Holt, "Evidence for Shock Acceleration of High Energy Electrons in the Supernova Remnant SN1006", *Nature*, Vol. 235, pp. 378-384, 1995.

3. Slane, P., J. P. Hughes, R. J. Edgar, P. P. Plucinsky, E. Miyata, H. Tsunemi, and B. Aschenbach, "RX J0852.0-4622: Another Nonthermal Shell Type Supernova Remnant (G266.2-1.2)", *Astrophysical Journal*, Vol. 548, No 2, pp. 814-819, 2001.

4. Borkowski, K. J., J. Rho, S. P. Reynolds and D. K. Kristy, "Thermal and Nonthermal X Ray Emission in Supernova Remnant RCW 86", *Astrophysical Journal*, Vol. 550, No. 1, pp. 334-345, 2001.

5. Bamba, A., R. Yamazaki, T. Yoshida, T. Terasawa and K. Koyama, "A Spatial and Spectral Study of Nonthermal Filaments in Historical Supernova Remnants Observational Results with Chandra", *Astrophysical Journal*, Vol. 621, pp. 793-802, 2004.

6. Decourchelle, A., D. C. Ellison and J. Ballet, "Thermal X Ray Emission and Cosmic Ray Production in Young Supernova Remnants", *Astrophysical Journal*, Vol. 543, pp. 57-60, 2000.

7. Bell, A. R., "The Acceleration of Cosmic Rays in Shock Fronts 2", *Monthly Notices of the Royal Astronomical Society*, Vol. 182, pp. 443-455, 1978.

8. Warren, J. S., J. P. Hughes, C. Badenes, P. Ghavamian, C. F. McKee, D. Moffett, P. P. Plucinsky, P. Rakowski, E. Reynoso and P. Slane, "Cosmic Ray Acceleration at the Forward Shock in Tycho's Supernova Remnant: Evidence from Chandra X

Ray Observations", *Astrophysical Journal*, Vol. 634, pp. 376-389, 2005.

9. Waxman, E., "High Energy Cosmic Rays from Gamma Ray Burst Sources: A Stronger Case", *Astrophysical Journal*, Vol. 606, No. 2, 2004.

10. Drury L. O. C., F. Aharonian and H. J. Völk, "The Gamma Ray Visibility of Supernova Remnants. A Test of Cosmic Ray Origin", *Astronomy and Astrophysics*, Vol. 376, pp. 959-971, 1994.

11. Ginzburg, V. L. and S. I. Syrovatskii, *The Origin of Cosmic Rays*, Oxford - Pergamon, New York, NY, USA, 1964.

12. Hillas, A. M., "Can Diffusive Shock Acceleration in Supernova Remnants Account for High Energy Galactic Cosmic Rays ?" *Physics Journal*, Vol. 731, pp. 95-131, 2005.

13. Rho, J. P., "Mixed-Morphology Supernova Remnants", *Astrophysical Journal*, Vol. 503, pp.167-168, 1998.

14. Rybicki, G. B. and A. P. Lightman, *Radiative Processes in Astrophysics*, Wiley-Interscience, New York, NY, USA, 1979.

15. Yamaguchi, H., *X Ray Study of Ejecta Dominated Supernova Remnants with Suzaku*, Ph.D. Thesis, Kyoto University, 2008.

16. Ozawa, M., *Study of Recombination X Rays from Supernova Remnants with Suzaku*, Ph.D. Thesis, Kyoto University, 2010.

17. Fowler, M., *Transforming Energy into Mass Particle Creation*, 2010, http://galileo.phys.virginia.edu/classes/252/particle-creation.html, accessed at May 2012.

18. Tolstoy, E., *Radiative Processes in Astrophysics-8 Bremsstrahlung*, 2008, http://www.astro.rug.nl/ etolstoy/astroa07/lecture8p.pdf, accessed at April 2012.

19. Garmire, G. P., M. W. Bautz, P. G. Fordb, J. A. Nouseka and G. R. Ricker, "Advanced CCD Imaging Spectrometer (ACIS) Instrument on the Chandra X Ray Observatory, X Ray and Gamma Ray Telescopes and Instruments for Astronomy", *Proceedings of the SPIE*, Vol. 4851, pp. 28-44, 2003.

20. Williams, B. S. and K. R. Gage, "The Chandra X Ray Observatory Mission Planning Process: Managing and Implementing Constraints", *Proceedings of the SPIE*, Vol. 6270, pp. 215-231, 2006.

21. Atwood, A. *et al.*, "The Large Area Telescope on the Fermi Gamma Ray Space Telescope Mission", *Astrophysical Journal*, Vol. 697, No. 2, pp. 1071-1102, 2009.

22. Nolan, P. L. *et al.*, "Fermi Large Area Telescope Second Source Catalog", *Astrophysical Journal*, Vol. 199, pp. 1108-1435, 2012.

23. Chevalier, R. and J. Oishi, "Cassiopeia A and Its Clumpy Presupernova Wind", *Astrophysical Journal*, Vol. 593, No. 1, pp. 23-26, 2003.

24. Reed, J. E., J. J. Hester, A. C. Fabian and P. F. Winkler, "The Three Dimensional Structure of the Cassiopeia A Supernova Remnant. I. the Spherical Shell", *Astrophysical Journal*, Vol. 440, pp.706-711, 1995.

25. Ballet, J., "X Ray Synchrotron Emission from Supernova Remnants", *Astrophysical Journal*, Vol. 244, pp. 144-167, 2005.

26. Sibthorpe, B. *et al.*, "Akari and Blast Observations of the Cassiopeia A Supernova Remnant and Surrounding Interstellar Medium", *Astrophysical Journal*, Vol. 719, pp. 1553-1564, 2010.

27. Rest, A. *et al.*, "Direct Confirmation of the Asymmetry of the Cas A Supernova with Light Echoes", *Astrophysical Journal*, Vol. 732, No. 1, pp. 1002-1051, 2011.

28. Vink, J. and J. M. Laming, "On the Magnetic Fields and Particle Acceleration in

Cassiopeia A", *Astrophysical Journal*, Vol. 584, pp. 758-769, 2003.

29. Hughes, J. P., "The Expansion of the X Ray Remnant of Tycho's Supernova (SN 1572)", *Astrophysical Journal*, Vol. 545, pp. 53-56, 2000.

30. Hwang, U., J. M. Laming, C. Badenes, F. Berendse and J. Blondin, "A Million Second Chandra View of Cassiopeia A", *Astrophysical Journal*, Vol. 615, pp. 117-120, 2004.

31. Long, K. S., S. P. Reynolds, J. C. Raymond, P. F. Winkler, K. K. Dyer and R. Petre, "Chandra CCD Imagery of the Northeast and Northwest Limbs of SN 1006", *Astrophysical Journal*, Vol. 586, pp. 1162-1178, 2003.

32. DeLaney, T. and L. Rudnick, "The First Measurement of Cassiopeia A's Forward Shock Expansion Rate", *Astrophysical Journal*, Vol. 589, pp. 818-826, 2003.

33. Aharonian, F. A. *et al.*, "Evidence for TeV Gamma Ray Emission from Cassiopeia A", *Astronomy and Astrophysics*, Vol. 370, No. 1, pp 431-462, 2001.

34. Uchiyama, Y. and F. A. Aharonian, "Fast Variability of Nonthermal X Ray Emission in Cassiopeia A: Probing Electron Acceleration in Reverse-Shocked Ejecta", *Astrophysical Journal*, Vol. 677, No. 2, pp. 105-108, 2008.

35. Krause, O., M. Tanaka, T. Usuda, T. Hattori, M. Goto, S. Birkmann and K. Nomoto, "Tycho Brahe's 1572 Supernova as a Standard Type-Ia as Revealed by Its Light-Echo Spectrum", *Nature*, Vol. 456, No. 7222, pp. 617-619, 2008.

36. Chevalier, R. A. and R. I. Klein, "Compact Models for Type I Supernovae", *Bulletin of the American Astronomical Society*, Vol. 11, pp. 725-728, 1979.

37. Reynoso, E. M., P. F. Velazquez, G.M. Dubner and W. M. Goss, "The Environs of Tycho's Supernova Remnant Explored through the H I 21 Centimeter Line", *Astrophysical Journal*, Vol. 117, No. 4, pp. 1827-1833, 1999.

38. Kothes, R., K. Fedotov, T. J. Foster and B. Uyaniker, "A Catalogue of Galactic Supernova Remnants from the Canadian Galactic Plane Survey. I. Flux Densities, Spectra, and Polarization Characteristics", *Astronomy and Astrophysics*, Vol. 457, No. 3, pp.1081-1093, 2006.

39. Katz-Stone, D. M., N. E. Kassim, T. Lazio, W. Joseph and R. O'Donnell, "Spatial Variations of the Synchrotron Spectrum within Tycho's Supernova Remnant (3C 10): A Spectral Tomography Analysis of Radio Observations at 20 and 90 Centimeter Wavelengths", *Astrophysical Journal*, Vol. 529, No. 1, pp. 453-462, 2000.

40. Katsuda, S., R. Petre, J. P. Hughes, U. Hwang, H. Yamaguchi, A. Hayato, K. Mori and H. Tsunemi, "X Ray Measured Dynamics of Tycho's Supernova Remnant", *Astrophysical Journal*, Vol. 709, No. 2, pp. 1387-1395, 2010.

41. Decourchelle, A., J. L. Sauvageot, M. Audard, B. Aschenbach, S. Sembay, R. Rothenflug, J. Ballet, T. Stadlbauer and R. G. West, "XMM Newton Observation of the Tycho Supernova Remnant", *Astronomy and Astrophysics*, Vol. 365, pp. 218-224, 2001.

42. Warren, J. S., J. P. Hughes and C. Badenes, "First Results from a Principal Component Analysis of Tycho's SNR: Evidence for Cosmic Ray Ion Acceleration", *Bulletin of the American Astronomical Society*, Vol. 37, pp.1437-1451, 2005.

43. Hayato, A., H. Yamaguchi, T. Tamagawa, S. Katsuda, U. Hwang, J. P. Hughes, M. Ozawa, A. Bamba, K. Kinugasa, Y. Terada, A. Furuzawa, H. Kunieda and K. Makishima, "Expansion Velocity of Ejecta in Tycho's Supernova Remnant Measured by Doppler Broadened X Ray Line Emission", *Astrophysical Journal*, Vol. 725, No. 1, pp. 894-903, 2010.

44. Allen, C. W., *Astrophysical Quantities*, the Athlone Press, London, UK, 1973.

45. Tian, W. W. and D. A. Leahy, "Tycho SN 1572: A Naked Ia Supernova Remnant Without an Associated Ambient Molecular Cloud", *Astrophysical Journal*, Vol. 729,

No. 2, pp. 15-32, 2011.

46. Giordano, F. *et al.*, "Fermi LAT Detection of the Young Supernova Remnant Tycho", *Astrophysical Journal*, Vol. 744, pp 32-37, 2012.

47. Acciari, A. *et al.*, "Discovery of TeV Gamma Ray Emission from Tycho's Supernova Remnant", *Astrophysical Journal*, Vol. 730, pp. 20-24, 2010.

48. Koyama, K., Petre, R., Gotthelf, E. V., Hwang, U., Matsuura, M., Ozaki, M. and Holt S., "Evidence for Shock Acceleration of High Energy Electrons in the Supernova Remnant SN1006", *Nature*, Vol. 378, No. 6554, pp. 255-258, 1995.

49. Del Rio, C. B., *Introduction to Binned Likelihood Analysis*, 2010, http://statistics.roma2.infn.it/ vitale/rep/likelihood_canadas.pdf, accessed at May 2012.

50. Hwang, U. *et al.*, "A Million Second Chandra View of Cassiopeia A", *Astrophysical Journal*, Vol. 615, No. 2, pp. 117-120, 2004.

51. Swordy, S., *Cosmic Ray Spectrum Picture*, 2002, http://astroparticle.uchicago.edu/siteold/cosmic_ray_spectrum_picture.htm, accessed at April 2012.

52. Seward, F., P. Slane and R. Smith, *Chandra Supernova Remnant Catalog*, 2012, http://hea_www.harvard.edu/ChandraSNR/snrcat_gal.html, accessed at April 2012.

53. Brandt, N., *Acis CCD Design*, 2008, http://www2.astro.psu.edu/ niel/astro485/lectures/lectures485.html, accessed at May 2012.

54. Lee, S., *HRC Shematic View*, 2008, http://chandra.harvard.edu/resources/illustrations/instruments_Schema.html, accessed at May 2012.

55. Lee, S., *Chandra Grating Spectrometers*, 2008,

http://chandra.harvard.edu/graphics/resources/illustrations/sci_illus-32l.jpg, accessed at May 2012.

56. Lee, S., *Chandra Spacecreaft Design*, 2008, http://chandra.harvard.edu/graphics/resources/illustrations/sci-illus-72l.jpg, accessed at May 2012.

57. Abdo, A. A. *et al.*, "Fermi-LAT Discovery of GeV Gamma Ray Emission from the Young Supernova Remnant Cassiopeia A", *Astrophysical Journal*, Vol. 710, No. 1, pp. 92-97, 2010.

58. Acciari, A. *et al.*, "Observations of the Shell Type SNR Cassiopeia A at TeV Energies with VERITAS", *Astrophysical Journal*, Vol. 714, pp. 163-169, 2010.

59. Völk, H. J., E. G. Berezhko and L. T. Ksenofontov, "Magnetic Field Amplification in Tycho and Other Shell Type Supernova Remnants", *29th International Cosmic Ray Conference Pune*, Vol. 3, p 233-236, 2005.

60. Rosswog, S. and M. Bruggen, *Introduction to High Energy Astrophysics*, Cambridge University Press, London, UK, 2007.

61. Aharonian, F. *et al.*, "Discovery of Gamma Ray Emission from the Shell Type Supernova Remnant RCW 86 with HESS", *Astrophysical Journal*, Vol. 692, pp. 78-89, 2009.